

See discussions, stats, and author profiles for this publication at: <https://www.researchgate.net/publication/357596316>

Experimental Aeroelastic Benchmark of a Very Flexible Wing

Article in AIAA Journal · January 2022

DOI: 10.2514/1.J060621

CITATIONS

12

READS

451

5 authors, including:



Daniella Raveh
Technion - Israel Institute of Technology

117 PUBLICATIONS 1,857 CITATIONS

[SEE PROFILE](#)



Ariel Drachinsky
Technion - Israel Institute of Technology

15 PUBLICATIONS 108 CITATIONS

[SEE PROFILE](#)



Moshe Tur
Tel Aviv University

765 PUBLICATIONS 20,385 CITATIONS

[SEE PROFILE](#)

Some of the authors of this publication are also working on these related projects:



Structural Health Monitoring (SHM) [View project](#)



Fiber optic based current sensing [View project](#)



Experimental Aeroelastic Benchmark of a Very Flexible Wing

Or Avin* and Daniella E. Raveh[†]

Technion—Israel Institute of Technology, 3200003 Haifa, Israel

Ariel Drachinsky[‡] and Yaron Ben-Shmuel[§]

Rafael, Advanced Defense Systems, 3102102 Haifa, Israel

and

Moshe Tur[¶]

Tel-Aviv University, 6997801 Ramat-Aviv, Israel

<https://doi.org/10.2514/1.J060621>

The paper presents the design, analyses, and testing of the Pazy wing, a very flexible wing model that was designed to study aeroelastic phenomena associated with geometrically nonlinear deflections and to provide data for validation of nonlinear aeroelastic simulation models. The Pazy wing is made of a main thin aluminum spar and a Nylon 12 printed ribs chassis providing the NACA0018 aerodynamic airfoil shape. The wing was covered entirely with a polyester film that serves as the skin. Static loading tests were used for model adaptation and to assure that the wing can deform to over 50% of its span without failing. Ground vibration tests were also used for model adaptation. Because there are uncertainties in the characteristics of the polyester skin under loads, both the static and ground vibration tests were used to assess the contribution of the skin to the wing's stiffness and determine the stiffness bound with and without the skin. Wind-tunnel tests were conducted at conditions that lead to static and unsteady structural responses. The wing deformations were tracked by a motion recovery system, and the strains over the wingspan were recorded with a Bragg-grating fiber-optics system. In the static wind-tunnel tests, the aerodynamic loads were recorded by a force balance. The wind-tunnel tests included angle-of-attack sweeps in constant airspeed and velocity sweeps in fixed angle of attack. The largest wing-tip static deformation recorded in test was of 50% span. In the velocity-sweep tests, the wing showed strong oscillations at a velocity at which the wing-tip deformation was approximately 25% of the span and became stable again at higher speeds. The wing models and test data are publicly available through the 3rd Aeroelastic Prediction Workshop (<https://nescacademy.nasa.gov/workshops/AePW3/public>).

I. Introduction

IN THE last decade, flight vehicles became increasingly more elastic. This is the case for unmanned aerial vehicles as well as for transport aircraft. For very flexible configurations, aeroelastic phenomena are exacerbated, and the industry-standard linear structural and aeroelastic models might no longer be adequate to accurately predict them. A notorious example is the Helios mishap [1], in which the technology demonstrator aircraft lost stability and crashed into the Pacific Ocean after deforming into a large dihedral shape in response to atmospheric turbulence. The Helios mishap investigation report [1] stated that the root causes of the mishap include the lack of appropriate analytical methods to predict the configuration's high sensitivity to disturbances that may lead to configurational changes and instability. Since then, there has been significant effort in the aeroelasticity community to develop and implement novel nonlinear models, in both the structure and aerodynamic disciplines, that can predict the nonlinear aeroelastic characteristics of flexible configurations in a broad range of flight conditions (see a review in Ref. [2]). A major area of research is in the development of nonlinear structural models that can accurately predict the response of very flexible configurations that undergo

large deformations. Examples of recent efforts are presented in Refs. [3–8].

An essential step in the maturation of novel nonlinear models is validation, which can be achieved through aeroelastic wind-tunnel or flight tests. Aeroelastic wind-tunnel tests can be used to assess the accuracy and validity of computational models and also to study phenomena beyond the current reach of theory. As aeroelastic wind-tunnel testing is complex, there are very few aeroelastic benchmarks available that target very flexible wing structures.

A seminal benchmark is that of Tang and Dowell [9], in which a rectangular, straight, high-aspect-ratio wing was tested in the subsonic wind-tunnel under static and dynamic loading conditions. This experimental study, published in 2001, is to date the only wind-tunnel benchmark on aeroelastic response of very flexible wings that offers the model and data, which can be used for model validation purposes. This benchmark wing is only marginally nonlinear, with maximal deformation in the order of 20% span, and the measured data are limited. Two recent studies [10,11] present the design and testing of very flexible, high-aspect-ratio wings. However, the models and data are not publicly available.

The current study presents the design, analysis, and testing of a new aeroelastic benchmark wing. The Pazy wing model is very flexible and experiences very large deformations, in the order of 50% span, under aerodynamic loading in the wind tunnel. Two wings of similar designs were constructed and tested in three wind-tunnel tests. The “Pre-Pazy” wing was tested mounted on a force balance and was destroyed in flutter. The Pazy wing was tested mounted to a force balance and directly to the wind-tunnel floor. While the Pre-Pazy and Pazy wings' designs are similar, their properties vary due to manufacturing tolerances and instrumentation (slightly affecting the inertia properties). The paper presents comprehensive experimental data of the Pazy wing. Some results of the Pre-Pazy wing are presented in the Appendix.

The experimental data include wind deformations measured by a motion recovery system (MRS), forces measured with a force balance (static data only), and strain measurements from fiber

Presented as Paper 2021-1709 at the 2021 AIAA SciTech Forum, Virtual Event, January 11–15 & 19–21, 2021; received 8 February 2021; revision received 2 August 2021; accepted for publication 25 August 2021; published online 27 December 2021. Copyright © 2021 by Yaron Ben-Shmuel and Moshe Tur. Published by the American Institute of Aeronautics and Astronautics, Inc., with permission. All requests for copying and permission to reprint should be submitted to CCC at www.copyright.com; employ the eISSN 1533-385X to initiate your request. See also AIAA Rights and Permissions www.aiaa.org/randp.

*Graduate Student, Faculty of Aerospace Engineering. Student Member AIAA.

[†]Professor, Faculty of Aerospace Engineering. Associate Fellow AIAA.

[‡]Research Associate. Member AIAA.

[§]Senior Research Associate.

[¶]Professor, School of Electrical Engineering.

Bragg grating (FBG) fiber-optic sensors (FOSs). While FOSs are routinely used for structural health monitoring of complex aerostructures, their usage in aeroelastic testing is relatively new [12–14]. FOS inherent capabilities, including strain accuracy comparable with that of standard electrical strain gauges, high sensitivity and wide strain dynamic range, high sampling rate (kilohertz for point sensing), multiplexed operation (one fiber can support many sensors), insensitivity to electromagnetic radiation, small size, and light weight, make FOSs highly suitable for aerospace systems. For the same reasons, FOSs are also very attractive for aeroelastic applications that require shape sensing. Recent studies demonstrated the experimental use of FOSs for measurement of a flexible wing's deformed shape [15,16] and aeroelastic dynamic characteristics [16,17]. Here, dynamic strain data are used to extract the wing's structural strain modes and to analyze the wing's aeroelastic characteristics with varying airspeed.

The study was carried out as part of the 3rd Aeroelastic Prediction Workshop (AePW). Its goal is to produce data for validation of geometrically nonlinear aeroelastic models and for assessing the capabilities and limitations of models of different order. The wing models and experimental data are available as open-source via the AePW.^{**} The experimental data include wing deformations, strains and aerodynamic coefficients.

II. Wing Design

The Pazy wing model was designed with the following requirements: 1) very large deformations in the order of 50% span under static aerodynamic loading, 2) measurement of elastic deformations and global aerodynamic coefficients, and 3) test at static conditions and flutter.

The design accounts for the following constraints: 1) wind tunnel speeds of 10–100 m/s and 2) test chamber dimensions of 1 by 1 m.

The Pazy wing has a chord length of 100 mm, a span of 550 mm, and a NACA0018 airfoil. It was designed to connect directly to the wind-tunnel chamber floor (Fig. 1a) or to connect to a force measurement device (force balance) via an adapter (Fig. 1b). The wing structure is made of an Aluminum 7075 spar, of dimensions 550 (length) by 60 (width) by 2.25 mm (thickness), and a Nylon 12, three-dimensionally printed chassis. The wing is covered with Oralight polyester film using an iron to activate the thermoactive adhesive, that is typically used in radio-controlled drones. The wing design is such that the main stiffness contributor (both in torsion and bending) is the aluminum plate, which provides about 85% of the stiffness. The aluminum plate is thin and thus experiences small strains.

A 300 mm long and 10 mm diameter wing-tip rod and a 120 mm diameter and 22 mm thick base are three-dimensionally printed as part of the chassis. The wing-tip rod is used for attaching weights (via drilled holes) that can modify the dynamic properties of the structure and alter the flutter characteristics. The base is used as an interface to connect the wing to the wind-tunnel floor or to the force balance adapter. Based on the CAD model and nominal material properties, the wing, without the base, weighs 328 g. Based on weighing, the wing weight with the accelerometer, wiring, and adhesives, the wing's actual weight is estimated as 361 g (without the segment of the main spar that protrudes the base).

The wing was assembled as follows:

- 1) At the base of the beam, two Aluminum 6061 fixtures were connected via two #8-32 bolts, as shown in Fig. 2.
- 2) The aluminum spar was inserted into the chassis until the aluminum fixtures touch the chassis's base (Fig. 3a).
- 3) The fixtures were fastened to the chassis base via three #8-32 bolts (Fig. 3b).
- 4) The aluminum spar was bonded to the chassis using LOCTITE 495 adhesive which was applied through holes on each rib.

^{**}Data available online at <https://nescacademy.nasa.gov/workshops/AePW3/public>.

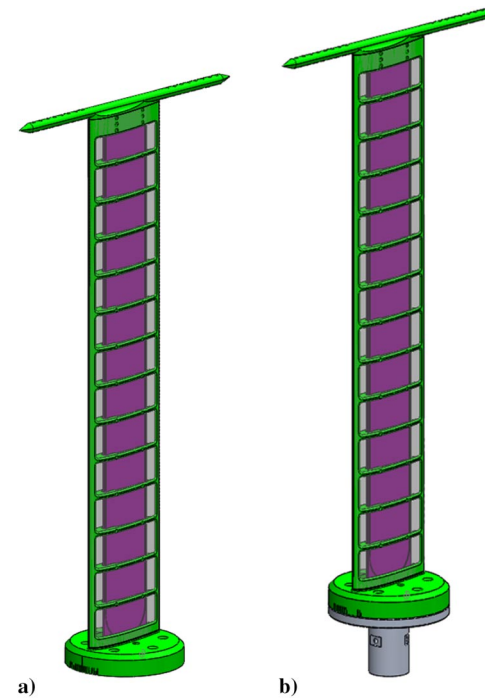


Fig. 1 Pazy wing CAD model a) without and b) with a force balance adapter.

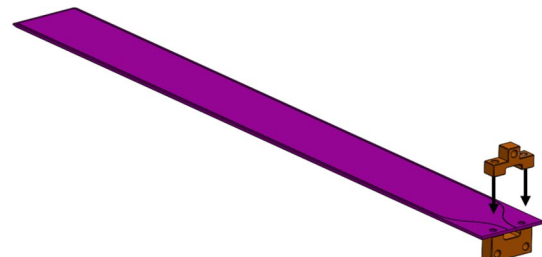


Fig. 2 Aluminum spar with brackets.

5) The chassis of the wing was covered with Oralight polyester film to produce a smooth aerodynamic surface.

The wing was modeled in SOLIDWORKS® software, and two finite element (FE) models were created: one in ANSYS® Workbench™ [18] and another in MSC Nastran. The ANSYS model was mainly used for stress analysis in the wing design process, while the Nastran model was used for free-vibration analysis. Both are presented in the following.^{††}

A. Stress Analysis

Stress analysis was performed in Ansys Mechanical, Release 17.0, as part of the wing design to verify that the wing can withstand the loads at the most severe test conditions. The Aluminum 7075 spar, Aluminum 6061 connection brackets, Nylon 12 base, chassis, and wing-tip rod were modeled using solid elements. The Oralight skin was modeled using shell elements. The #8-32 bolts were modeled using beam elements. The LOCTITE 495 adhesive was modeled as bonded contacts between the aluminum spar and the Nylon 12 chassis. Table 1 presents the nominal material properties, as provided

^{††}ANSYS, ANSYS Workbench, AUTODYN, CFX, FLUENT, and any and all ANSYS, Inc., brand, product, service and feature names, logos, and slogans are registered trademarks or trademarks of ANSYS, Inc., or its subsidiaries in the United States or other countries. All other brand, product, service, and feature names or trademarks are the property of their respective owners.

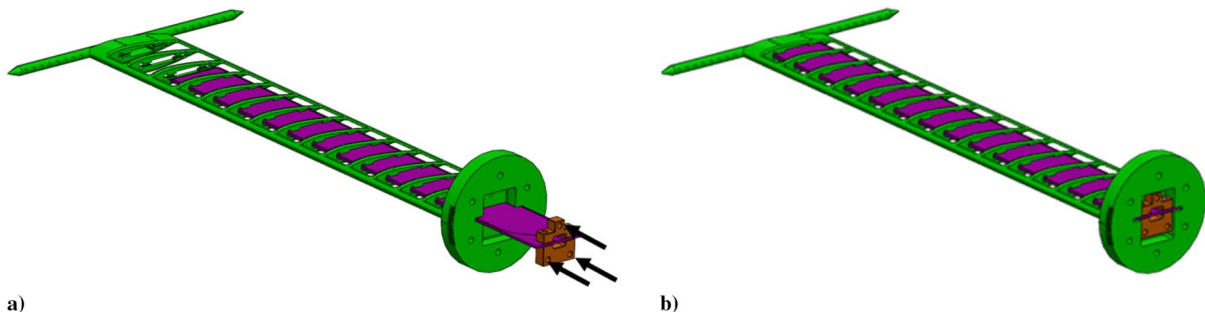


Fig. 3 Wing final assembly procedure: a) inserting the beam into the chassis and b) fastening the brackets into the chassis.

Table 1 Nominal material properties

Material	Density	Young's modulus, MPa	Poisson's ratio	Yield strength, MPa	Tensile strain, %
Aluminum 7075-T6	2795 (kg/m ³)	71000	0.33	468	8
Aluminum 6061-T651	2712 (kg/m ³)	71000	0.33	245	10
Nylon 12	930 (kg/m ³)	1700	0.394	48 ^b	25
Oralight ^a	36 (g/m ²)	4666	0.4	80	25

^aMaterial properties derived from tensile test; see Appendix A.

^bFlexural strength: 58 MPa.

by the manufacturer. The properties in the FE models were adjusted following adaptation tests (Sec. IV).

For the stress analysis, the load was modeled as a concentrated force of 75.7 N at 40% span and 25% chord of the wing. This force creates root bending and torsion moments that are equal to those created by the aerodynamic loading at 55 m/s, 7 deg root angle of attack, as predicted by the modal rotation method (MRM) nonlinear aeroelastic analysis [19]. Because of convergence issues related to the skin's lack of compression stiffness, the wing was analyzed with the skin modeled only on the tensioned side. The nonlinear analysis accounted for large deformations and the skin's plasticity.

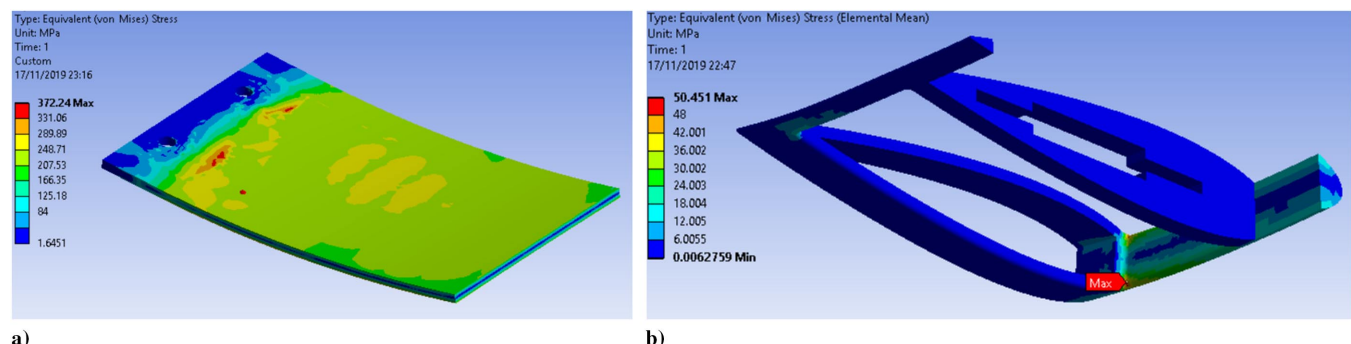


Fig. 4 Stress analysis results: a) aluminum spar root and b) Nylon 12 chassis base.

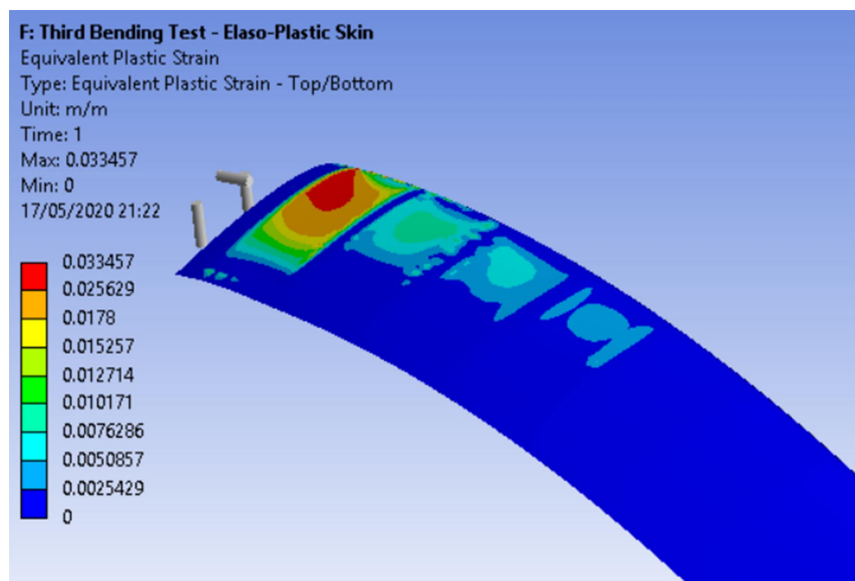


Fig. 5 Stress analysis results: Oralight skin plastic strain.

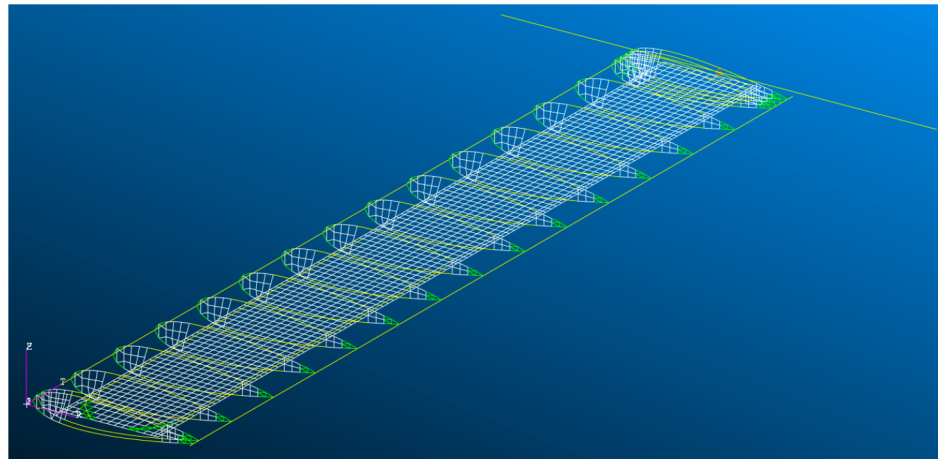


Fig. 6 Finite element model.

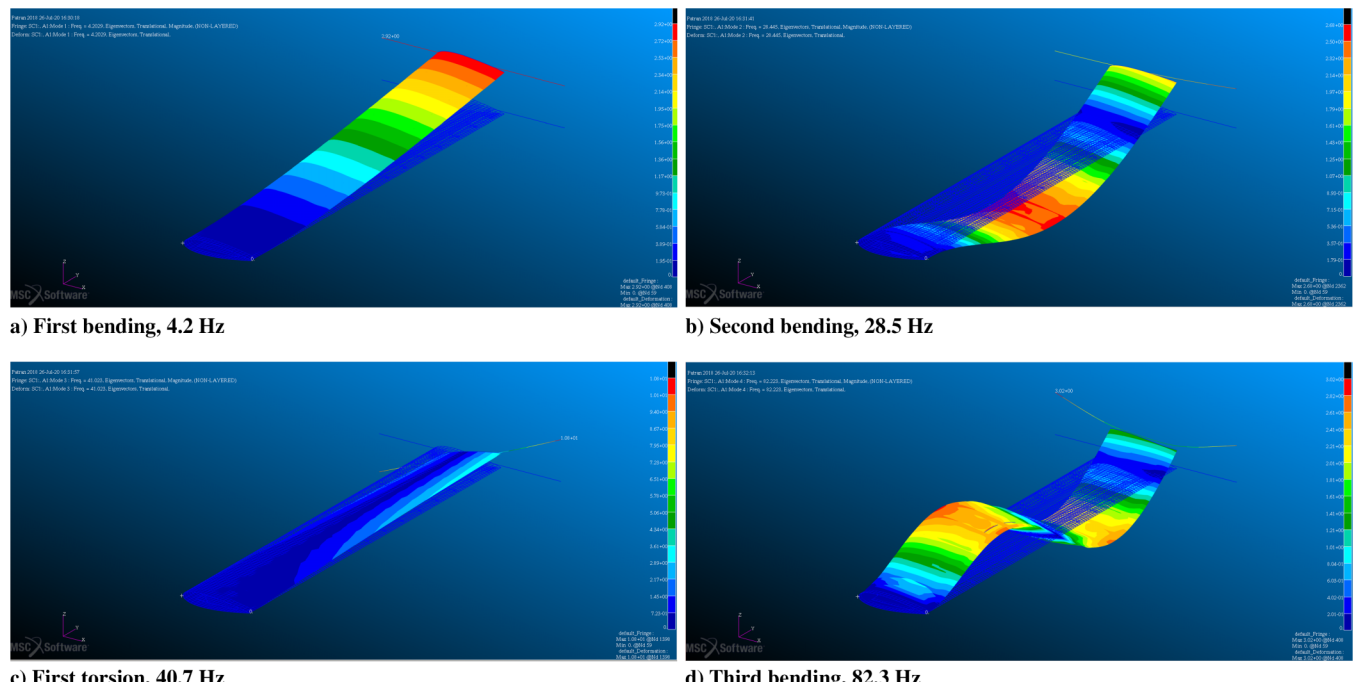


Fig. 7 First four mode shapes and frequencies of the Pazy wing with skin (LE = Leading Edge; TE = Trailing Edge).

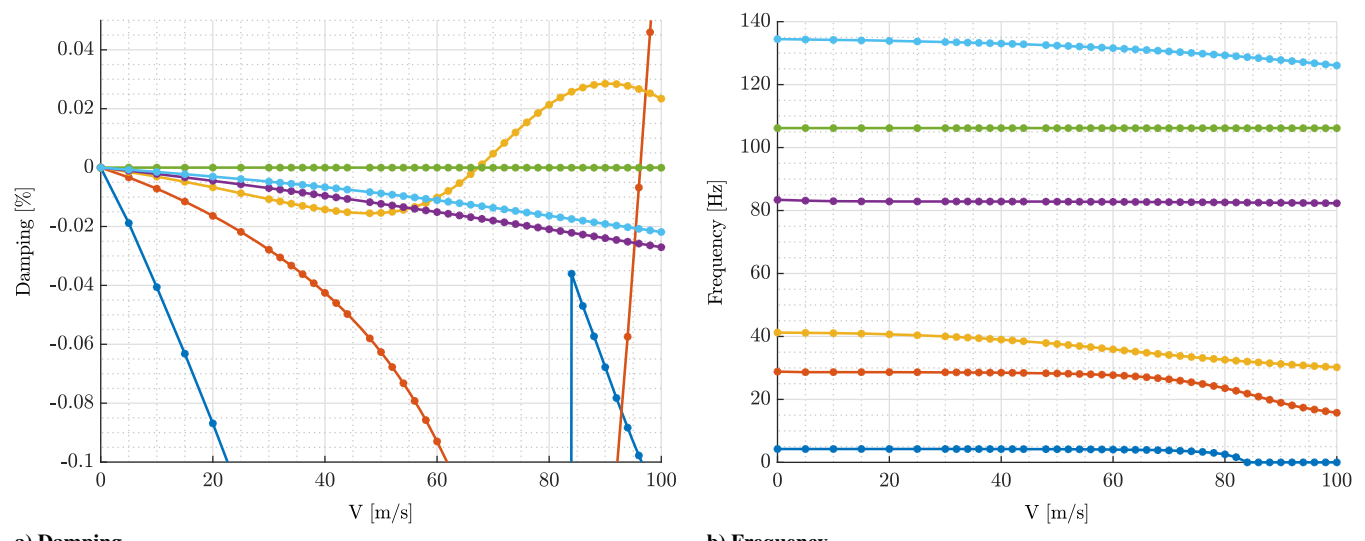


Fig. 8 ω – V – g plot, presenting the variation of the frequencies and damping as a function of airspeed.

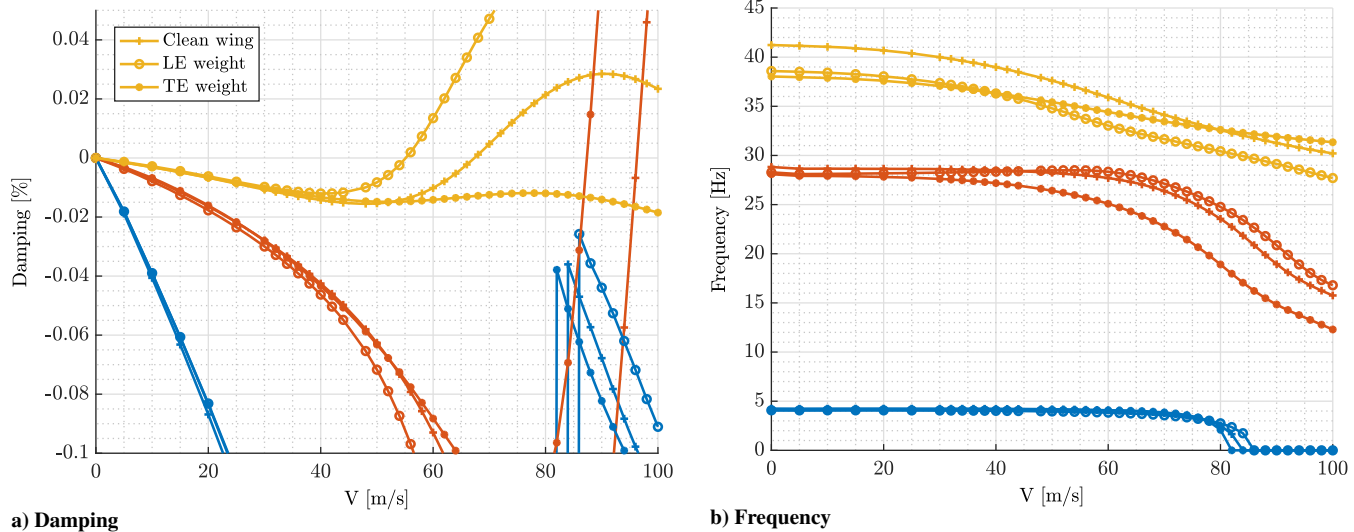


Fig. 9 $\omega - V - g$ plot for the clean wing and for the wing with a leading- and trailing-edge 10 g weight configurations.

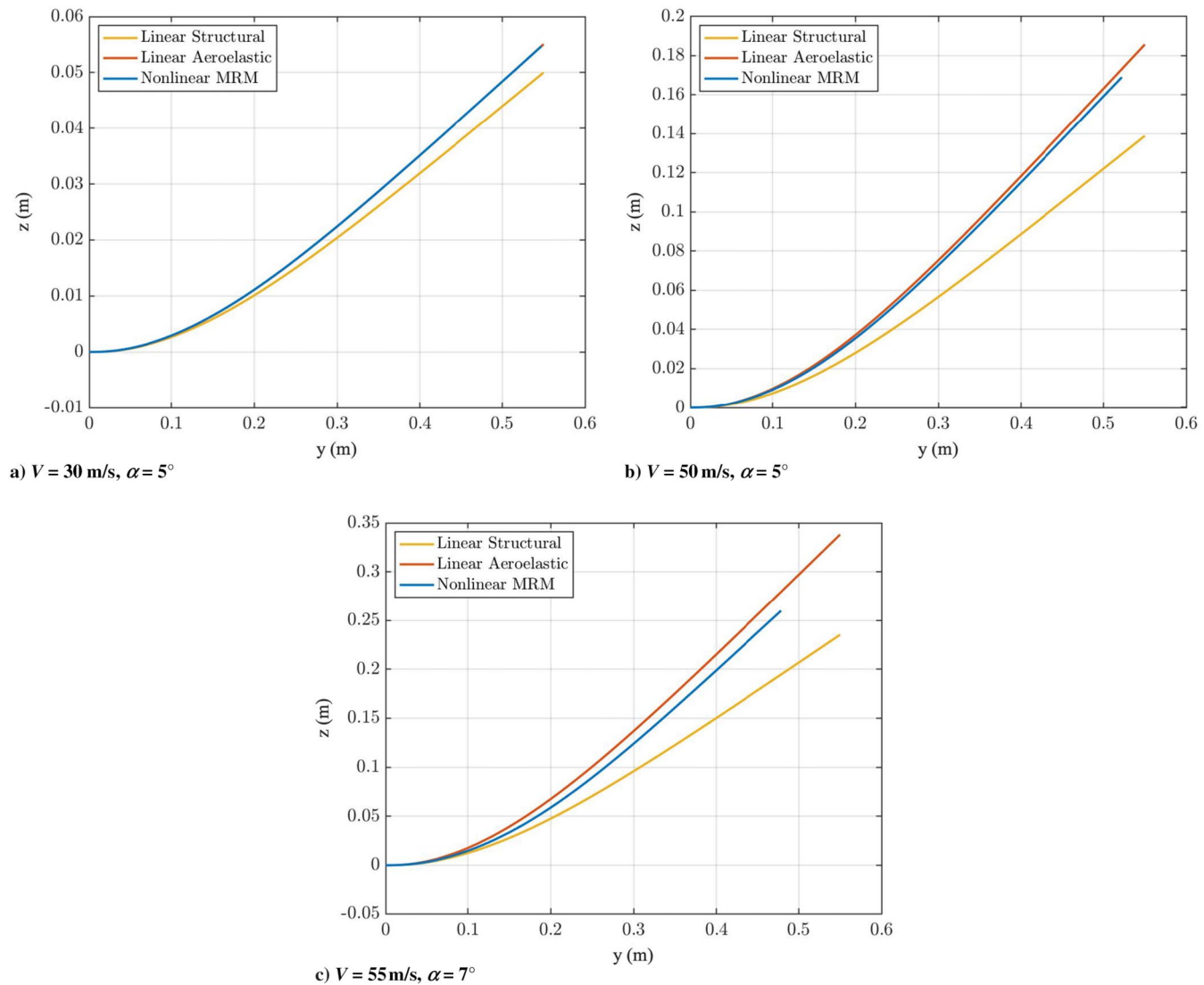


Fig. 10 Computed wing deformations for three wind-tunnel conditions resulting in a) linear small deformations, b) large deformations, and c) very large deformations.

Table 2 Computed wing-tip deformation at static loading conditions

Deformation	AOA, deg	V, m/s	Tip deformation, mm	Twist, deg	Incremental AOA, deg
Linear, small	5	30	50 (9% span)	0.6	0.6
Large	5	50	170 (31% span)	1.8	1.6
Very large	7	55	260 (47% span)	2.8	1.7

Three main stress areas were identified: one at the root of the aluminum spar, one near the base of the Nylon 12 chassis (Fig. 4), and one at the root of the Oralight skin, between the first and second ribs (Fig. 5). The maximum stress computed in the aluminum spar is 372 MPa, which corresponds to a safety factor of 1.25. The computed stress in the Nylon 12 chassis is between the reported tensile and flexural strength values for the Nylon 12 material. There might be

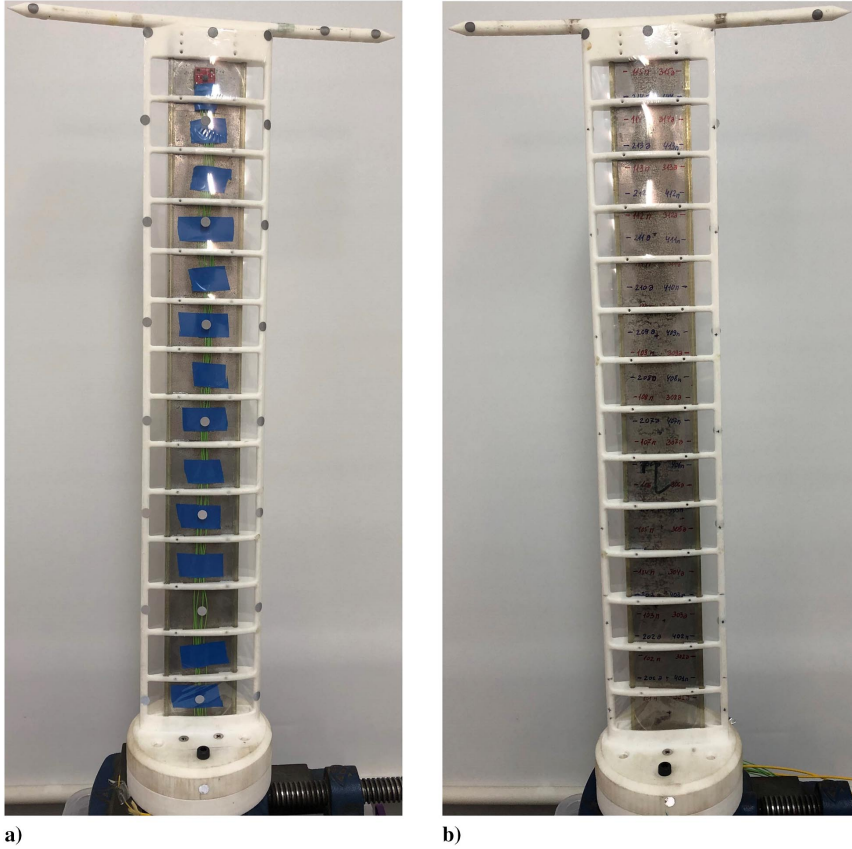


Fig. 11 Instrumented wing: a) MRS IR reflectors and b) FBG strain sensors.

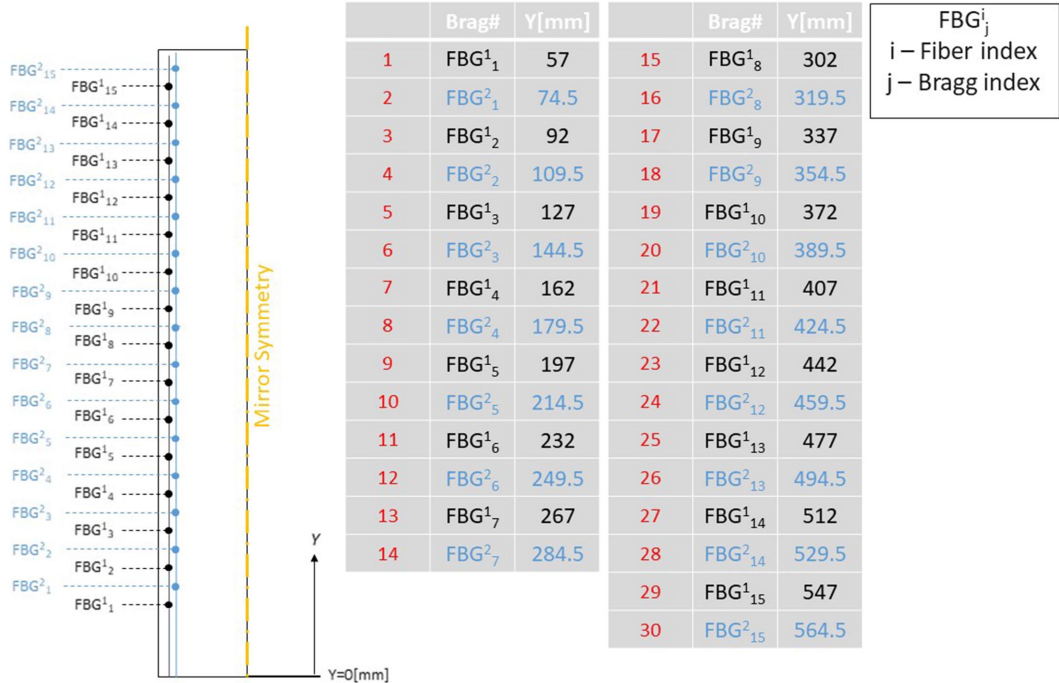


Fig. 12 FBG strain sensors scheme.

Table 3 GVT M+P data for the wing with skin; measured in an upright position

Mode	Frequency, Hz	Damping ratio
Data (Method)	Accelerometers	Accelerometers
First bending	4.26	0.002
Second bending	28.5	0.005
First torsion	42.0	0.0045
In-plane bending	60.7	0.006
Third bending	81.5	0.007

Table 4 GVT data for the wing with skin; measured in horizontal position

Mode	Frequency, Hz	Frequency, Hz	Frequency, Hz
Data (Method)	Disp. (PSD)	Disp. (SPOD)	Strains (PSD)
First bending	4.48	4.69	4.39
Second bending	29.4	30.0	29.8
First torsion	41.0	41.3	41.0
Third bending	81.3	81.6	82.5

Disp. = Displacements.

Table 5 GVT data for the wing without skin; measured in horizontal position

Mode	Frequency, Hz	Frequency, Hz	Frequency, Hz	Frequency, Hz
Data (Method)	Disp. (PSD)	Disp. (SPOD)	Strains (PSD)	Strains (SPOD)
First bending	4.2	4.2	4.2	4.2
Second bending	29.1	29.0	29.2	29.3
First torsion	39.8	39.9	40.0	40.0
Third bending			80.6	

local yielding at the root area, which is contained and not expected to affect the global stiffness. The maximum stress in the Oralight skin is 128 MPa, exceeding the yield stress of 80 MPa. The maximum computed total strain (e.g., elastic and plastic strain) in the Oralight skin is 7.2%, which is above the yield strain of 1.78% but an order of magnitude less than the ultimate tensile strain, which is above 25%. The resulting plasticity of 3.3% in the Oralight skin can be seen in Fig. 5. This implies that, although the skin will not fail under these loads, between the first two ribs its contribution to the wing's bending stiffness will decrease.

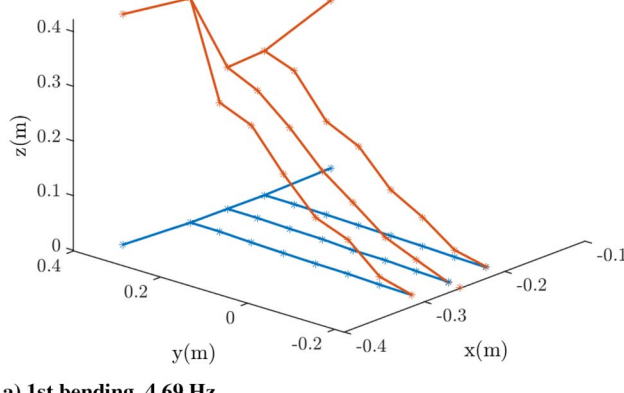
III. Free-Vibrations and Aeroelastic Analyses

Figure 6 shows the MSC Nastran FE model that was used for the structural and aeroelastic analyses. The aluminum spar is modeled with plate elements and the nylon parts are modeled using plate and beam elements. The polyester skin, not shown in Fig. 6, was modeled with plate elements. The wing root is clamped.

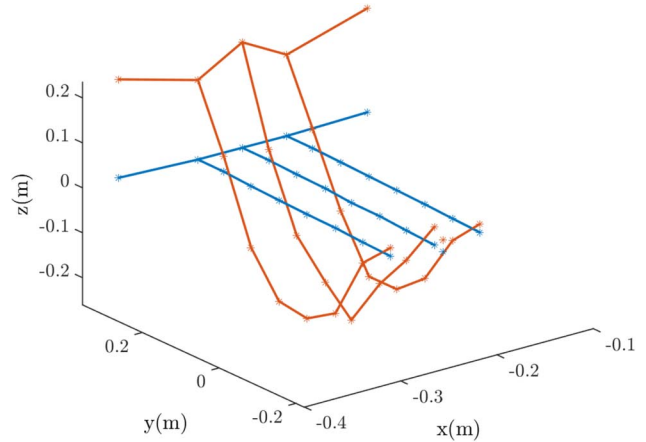
Two models were adapted: a model of the wing without the Oracover skin and a model with the skin and with an additional weight representing the accelerometer that is attached at the wing-tip centerline. The Nylon 12 and Oralight material Young's modulus were set to 1100 and 467 MPa, respectively, to adapt the model based on static loading and ground vibration test (GVT) results (reported in Sec. IV). A weight of 10 g was added at the wing-tip centerline for frequencies calibration, and an additional 5 g weight was added at the same location to account for the accelerometer (in the skin-on model only).

A. Free-Vibration Analysis

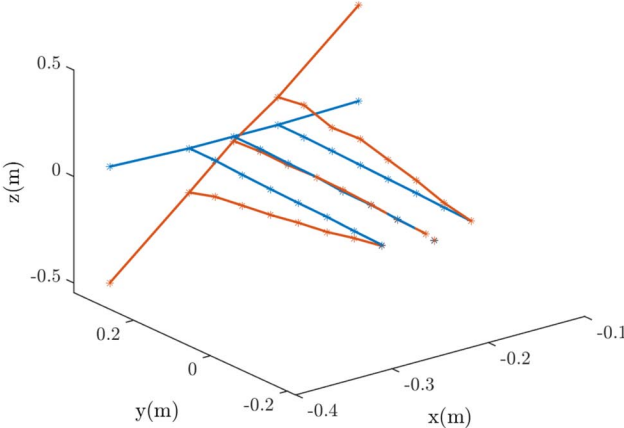
Linear free-vibration analysis provided the structure's natural frequencies and mode shapes, which were then used for flutter



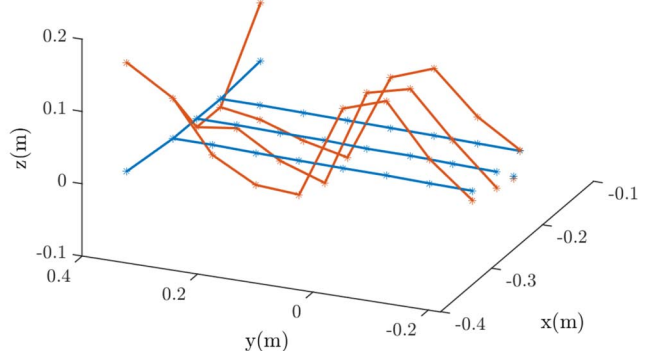
a) 1st bending, 4.69 Hz



b) 2nd bending, 30.0 Hz



c) 1st torsion, 41.3 Hz



d) 3rd bending, 81.6 Hz

Fig. 13 Displacement modes identified in the GVT from displacement data; wing in horizontal position.

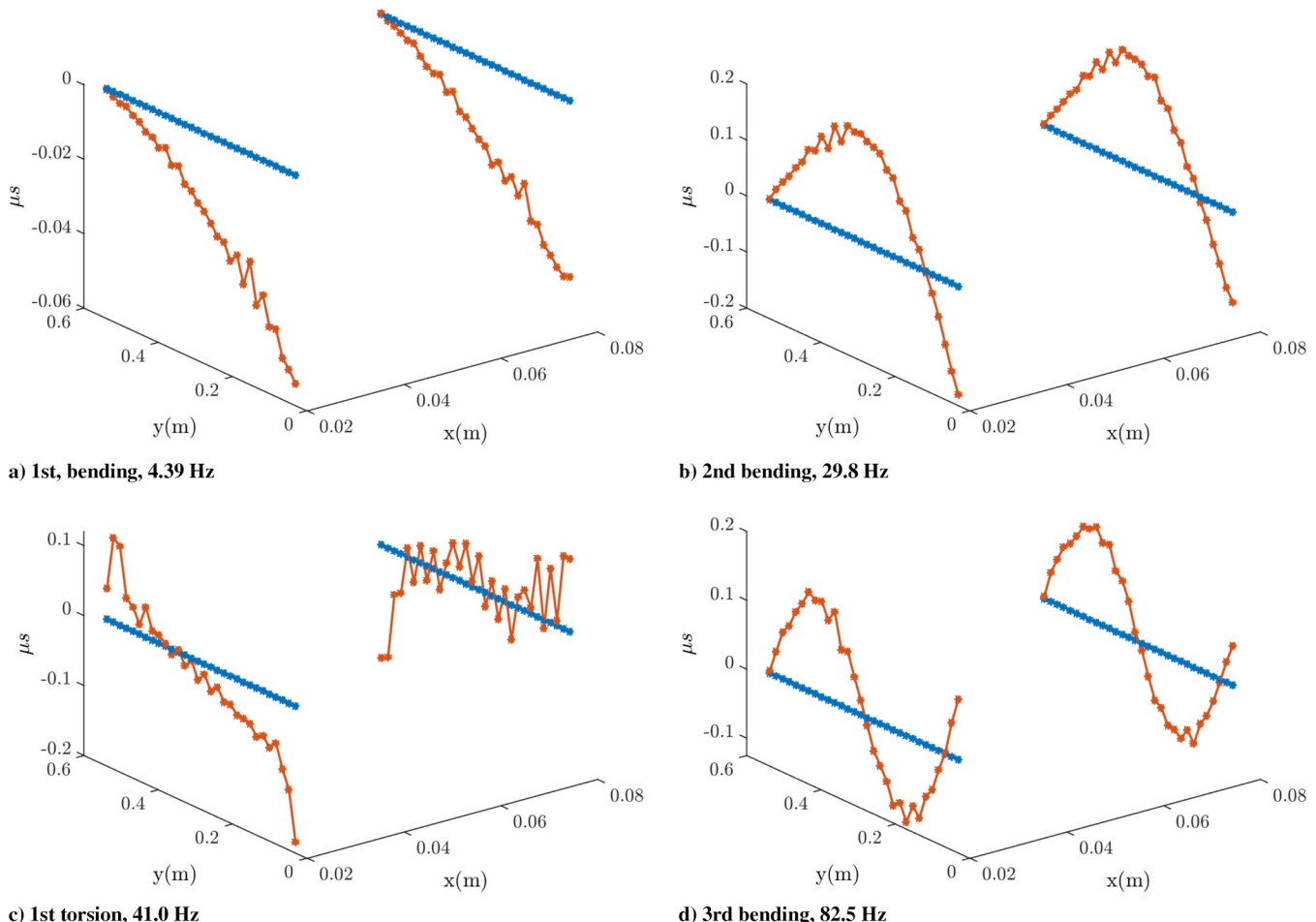


Fig. 14 Strain modes identified in the GVT from FBG sensor data; wing in horizontal position.

Table 6 GVT data measured on the wing with skin; installed in the wind-tunnel compared to FE model frequencies

Mode	Frequency, Hz	Frequency, Hz	Frequency, Hz
Data (Method)	FE model	Disp. (SPOD)	Strains (SPOD)
First bending	4.2	4.22	4.17
Second bending	28.5	28.1	28.3
First torsion	40.7	41.3	41.3
Third bending	82.3		81.5

analysis and as the basis for the nonlinear aeroelastic analysis using the MRM [8,19]. Figure 7 shows the first four low-frequency modes of the wing with skin on and their corresponding frequencies, following model calibration.

B. Linear Flutter Analysis

Linear flutter analysis was performed using the ZAERO aeroelastic analysis software based on a linear panel aerodynamic model [20]. The wing surface was divided into 20 and 40 panels in the chordwise



Fig. 15 Static loading test setup: a) bending and b) coupled bending–torsion.

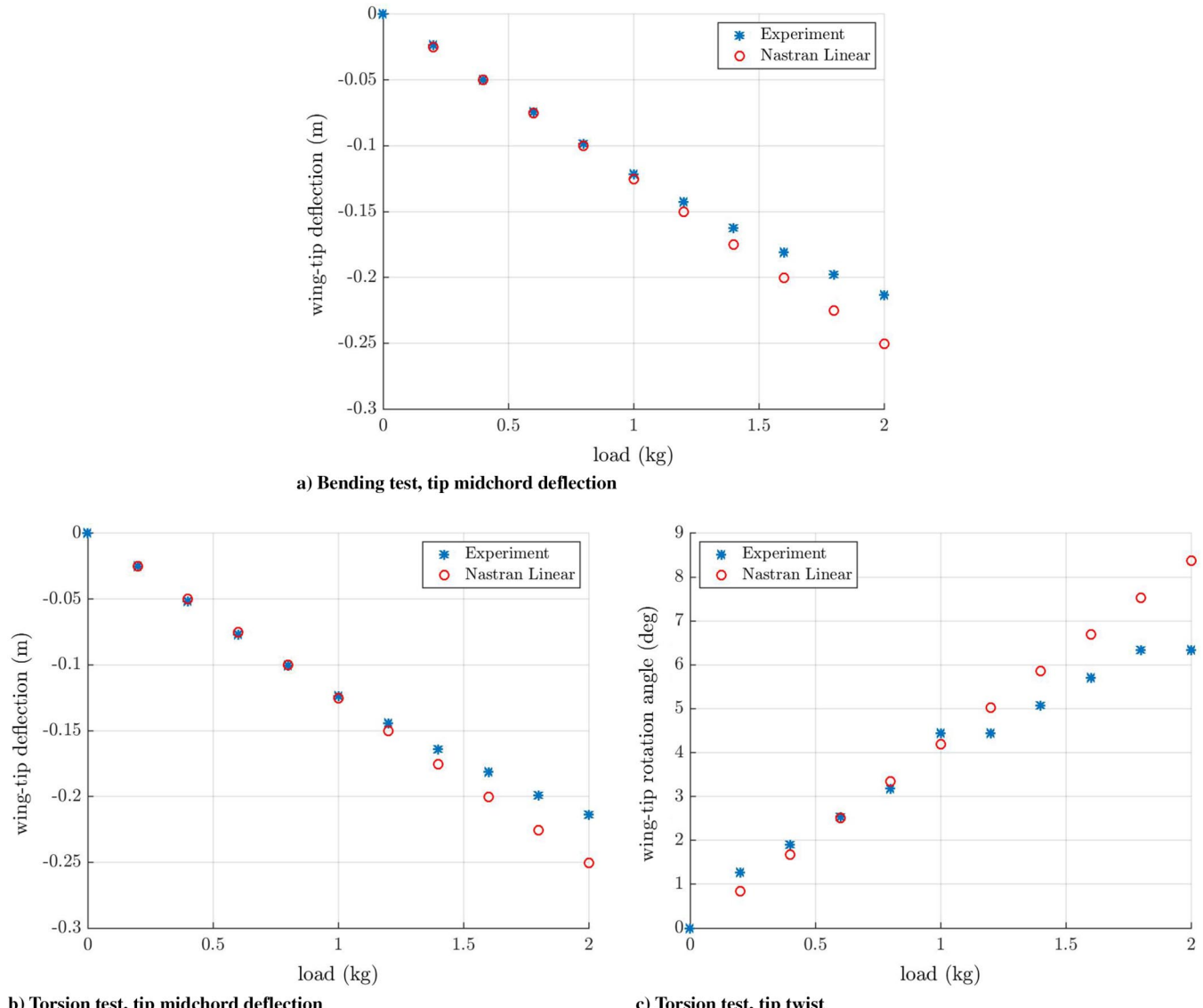


Fig. 16 Comparison of computational and experimental results for static loading of the wing without skin: a) Pure bending test and b,c) coupled bending and torsion test.

and spanwise directions, respectively. Figure 8 shows the $\omega - V - g$ plot, presenting the variation of the frequencies and damping as a function of airspeed. Flutter onset was computed at 67 m/s and a frequency of 34.5 Hz. The flutter mode is a hump mode combination of first torsion and second bending. Divergence instability appears at 83 m/s and an additional flutter instability, involving the first bending and first torsion modes, is computed at 96 m/s and a frequency of 16.7 Hz. Flutter analysis was based on the first ten low-frequency modes. Only the first six are shown in Fig. 8. The in-plane bending mode, at 106 Hz in the FE model, does not contribute to the linear aeroelastic interaction.

A 10 g weight was added to the wing tip, 10 mm ahead of the leading edge or 10 mm behind the trailing edges to examine its effect on flutter onset. Flutter analyses results (Fig. 9) indicate that, unlike in a classical first torsion–first bending mechanism, in which a forward weight delays flutter onset, here, the addition of a forward weight results in an early, more abrupt flutter at 55 m/s and 33.8 Hz. This is due to the reduction of the torsion mode frequency with airspeed. The reduction of the torsion frequency is also responsible for this flutter mechanism being a hump mode, as in higher airspeeds the torsion frequency is reduced below that of the second bending.

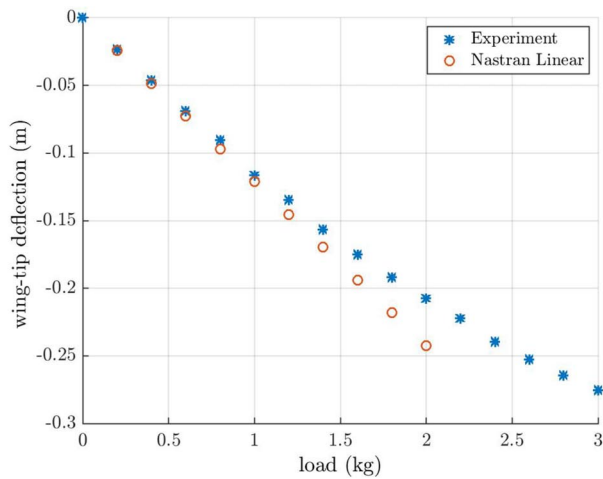
A trailing-edge weight delays flutter onset and makes the first-torsion second-bending hump mode flutter. Addition of a 10 g

trailing-edge weight completely eliminates this mechanism. Instead, an abrupt first-bending first-torsion mechanism appears at 87 m/s and 15.7 Hz. According to these findings, the wind-tunnel tests were conducted with a 10 g weight attached at the trailing edge or behind it.

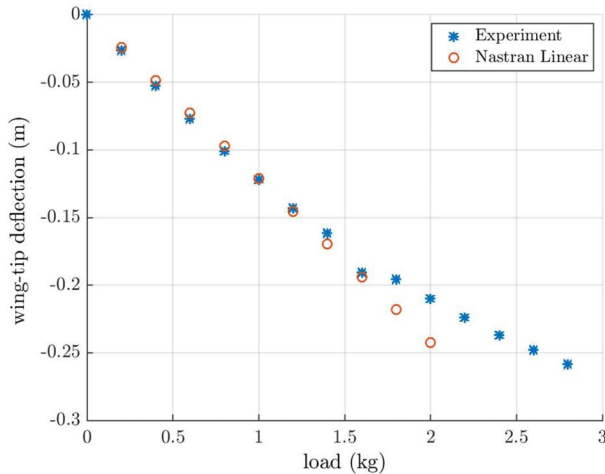
C. Nonlinear Static Aeroelastic Analysis

Wing deformations were computed with the MRM [8,19], accounting for nonlinearities due to large structural displacements. The rigid aerodynamic load distribution over the wingspan was computed by ZAERO and aeroelastically corrected to account for the local angle of attack (AOA) due to elastic wing twist and bending rotation. Detailed MRM-based aeroelastic analyses of the Pazy wing are presented in Ref. [19].

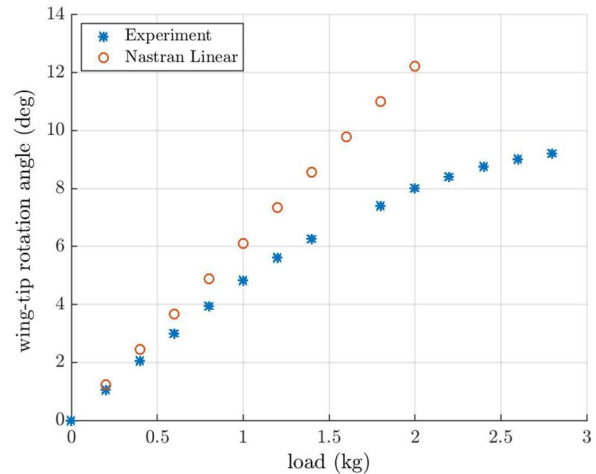
Although in the wind-tunnel experiment multiple airspeeds and AOA combinations were tested, we focused the analyses on the following three static conditions to design and guide the experiments: 1) 5 deg AOA, 30 m/s (a low root AOA, low dynamic pressure case that leads to small deformations); 2) 5 deg AOA, 50 m/s (a low root AOA, high dynamic pressure case that yields large deformations); and 3) 7 deg AOA, 55 m/s (a higher root AOA, high dynamic pressure case that yields very large deformations).



a) Bending test, tip midchord deflection

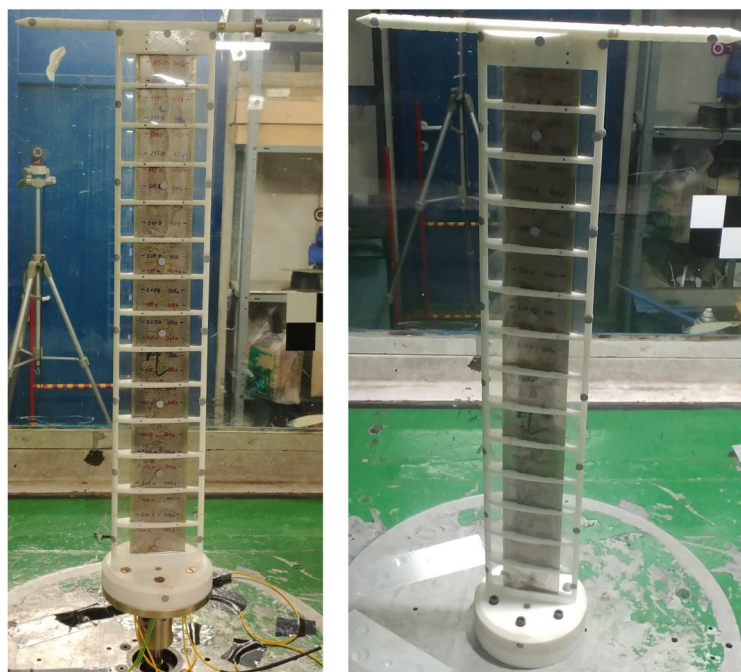


b) Torsion test, tip midchord deflection



c) Torsion test, tip twist

Fig. 17 Comparison of computational and experimental static loading test results for the wing with skin: a) Pure bending test and b,c) coupled bending and torsion test.



a) Test 1 : force balance

b) Test 2 : tunnel floor

Fig. 18 Wind-tunnel tests setups: a) test 1 and b) test 2.



Fig. 19 A 10 g weight added 40 mm behind the trailing edge to increase the flutter onset speed.

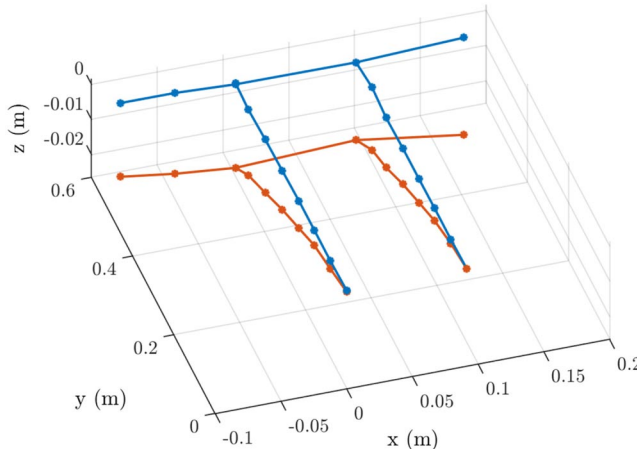


Fig. 20 MRS sensor locations in the initial state (red stars) compared to their locations on a theoretical, undeformed wing (in blue); wind-tunnel test 1.

Figure 10 shows wing deformations (out-of-plane displacements of the wing's centerline) computed for the three loading cases. Each figure shows the deformed wing as computed by a linear structural analysis assuming a fixed rigid load (labeled *Linear Structural*), a linear aeroelastic analysis accounting for the elastic sectional AOA (labeled *Linear Aeroelastic*), and a MRM nonlinear analysis. In the MRM analysis, the aerodynamic forces are computed for the deformed shape assuming linear aerodynamics.

Table 2 presents the wing-tip deformation, twist angle, and sectional incremental AOA (i.e., the local AOA minus the rigid AOA) corresponding to these cases.

IV. Structural Tests

Structural tests included static loading tests and a GVT. In these tests, wing deformations were captured by an OptiTrack^{##} MRS. The MRS system consists of three Flex 13 cameras that track infrared markers taped onto the wing. The system measures translations in X, Y, and Z directions, defined during the initial calibration procedure (X is the chord direction, Y is the wingspan direction, and Z is the out of plane direction).

Twenty-four infrared reflector stickers were attached to the wing, over the leading and trailing edges and the center chord (Fig. 11a). Three additional reflectors were attached to the wingtip bar. The deformation data were used to indicate the deformed shape in the static loading tests, and their frequency analysis was used in the GVT.

According to the manufacturer, the Flex 13 delivers submillimeter marker precision. Thus, under static load, we considered the error to be in the order of 1 mm. For the dynamic tracking under no load, the average 6σ deviation of the out-of-plane measurement of all the reflectors was computed to be 0.14 mm.

The wing was instrumented with strain-measuring optical fibers. Four optical fibers with inscribed Bragg gratings were affixed to one surface of the aluminum spar, providing strain measurement at 30 points over each of the leading and trailing edges of the spar. The

four fibers were set into two 1 mm wide and 0.1 mm deep cavities along the length of the aluminum spar, located at 22 mm from the leading edge and at 21.3 mm from the trailing edge. Because of hardware limitations, each fiber has 16 discrete FBGs sensors spaced 35 mm apart. Two fibers were placed in each cavity, with a shift of 17.5 mm between sensor locations, providing an array of 30 FBG sensors on each side. Each of the four FBG arrays has its last member free, in other words, not embedded to the aluminum spar but enclosed in the wing tip, providing temperature measurement. The fibers were glued to the aluminum spar with 3M-DP100 adhesive. Figure 11b shows the FBG sensor locations marked in red and blue (on the two fibers). Figure 12 shows a schematic view of the FBG sensors' locations along the aluminum spar (only one side is shown due to symmetry).

In principle, FBG is sensitive to both strain and temperature. In the current study, the fibers were in very good thermal contact with the aluminum spar, which constitutes a fairly large thermal bath. Temperature measurements indicate that temperature changes are very slow so they do not affect dynamic measurements.

The average 6σ deviation of the strain measurements of all the FBG sensors was computed to be $7.2(\mu\epsilon)$. This was estimated from a time-history of the FBG sensors measured when the wing was unloaded.

A. Modal Tests

Several GVTs were carried out on the wing with and without skin, based on different measured data (accelerations, displacements, and strains) and using different analysis techniques. A GVT for the wing with the skin was performed with an M+P system^{§§} based on frequency response functions between measured accelerations and a force input by an instrumented modal hammer. Because of the flexibility of the wing, the driving (excitation) point was set at 33% span, at the leading edge such that the deformations were kept small throughout the excitation. One to eight accelerometers were attached to the wing. Sensitivity checks ensured that all modes up to 100 Hz were excited and that the added mass of the accelerometers (1 g each) did not affect the results. Modes and frequencies were extracted using the P-LSCF algorithm [21] as implemented in the M+P software. The GVT provided the first five frequencies and damping ratio values of the wing, shown in Table 3. It is noted that the wing has very little structural damping.

A GVT was also performed for the wing with and without the skin in a horizontal position to estimate the contribution of the skin to the wing's stiffness. Modal frequencies were extracted from responses to a slight hit at the wing tip based on output-only data. The wing's displacement response was tracked by the MRS (at 240 Hz), and the strains were tracked by the FBG sensors (at 1000 Hz). The data were filtered below 2 Hz and above 100 Hz. The frequencies were extracted by Welch's power spectral density (PSD) estimate, using ten windows with 80% overlap. Frequencies and mode shapes were also computed using the spectral proper orthogonal decomposition (SPOD) algorithm [22]. Frequencies of the wing with and without the skin are reported in Tables 4 and 5, respectively.

Comparing the skin-on and skin-off data, the polyester skin slightly stiffens the wing, increasing the first bending frequency in approximately 5% and the first torsion in approximately 3%. It is noted that the first bending frequency measured for the wing in the horizontal position is slightly higher and the torsion is slightly lower than for the vertical wing. This could be possibly attributed to the contribution of the stretched skin when in a horizontal position. In the wind-tunnel test, the wing was in a vertical position.

SPOD [22] was used to extract the displacement and strain mode shapes from the displacements and strain data, respectively. Figure 13 shows the first four displacement mode shapes identified from a single response case for the wing in the horizontal position. The

^{##}Data available online at <http://optitrack.com> [retrieved 20 November 2021].

^{§§}Data available online at <https://www.mpihome.com/en/products/dynamic-signal-analysis/modal-analysis.html> [retrieved 20 November 2021].

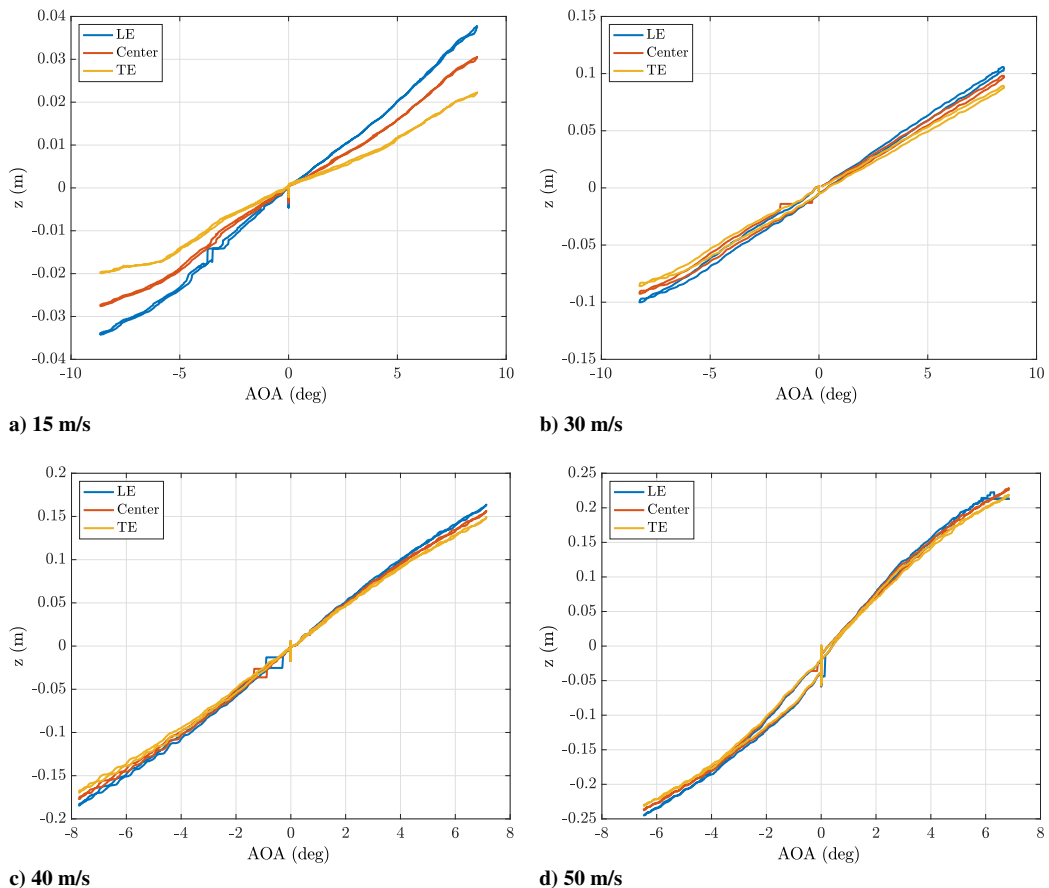


Fig. 21 Wing-tip normal deformations at the leading edge (LE), center chord (Center), and trailing edge (TE) during AOA sweeps; wind-tunnel test 1.

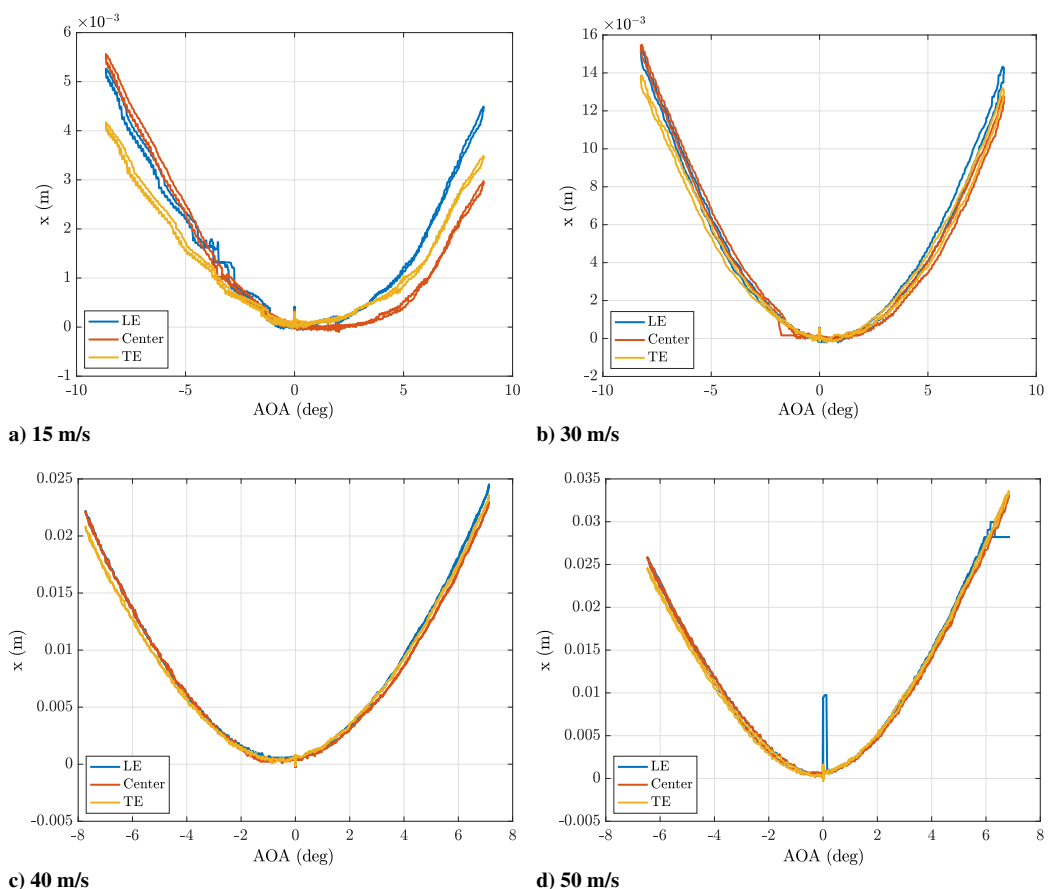


Fig. 22 Wing-tip chordwise deformations at the leading edge (LE), center chord (Center), and trailing edge (TE) during AOA sweeps; wind tunnel test 1.

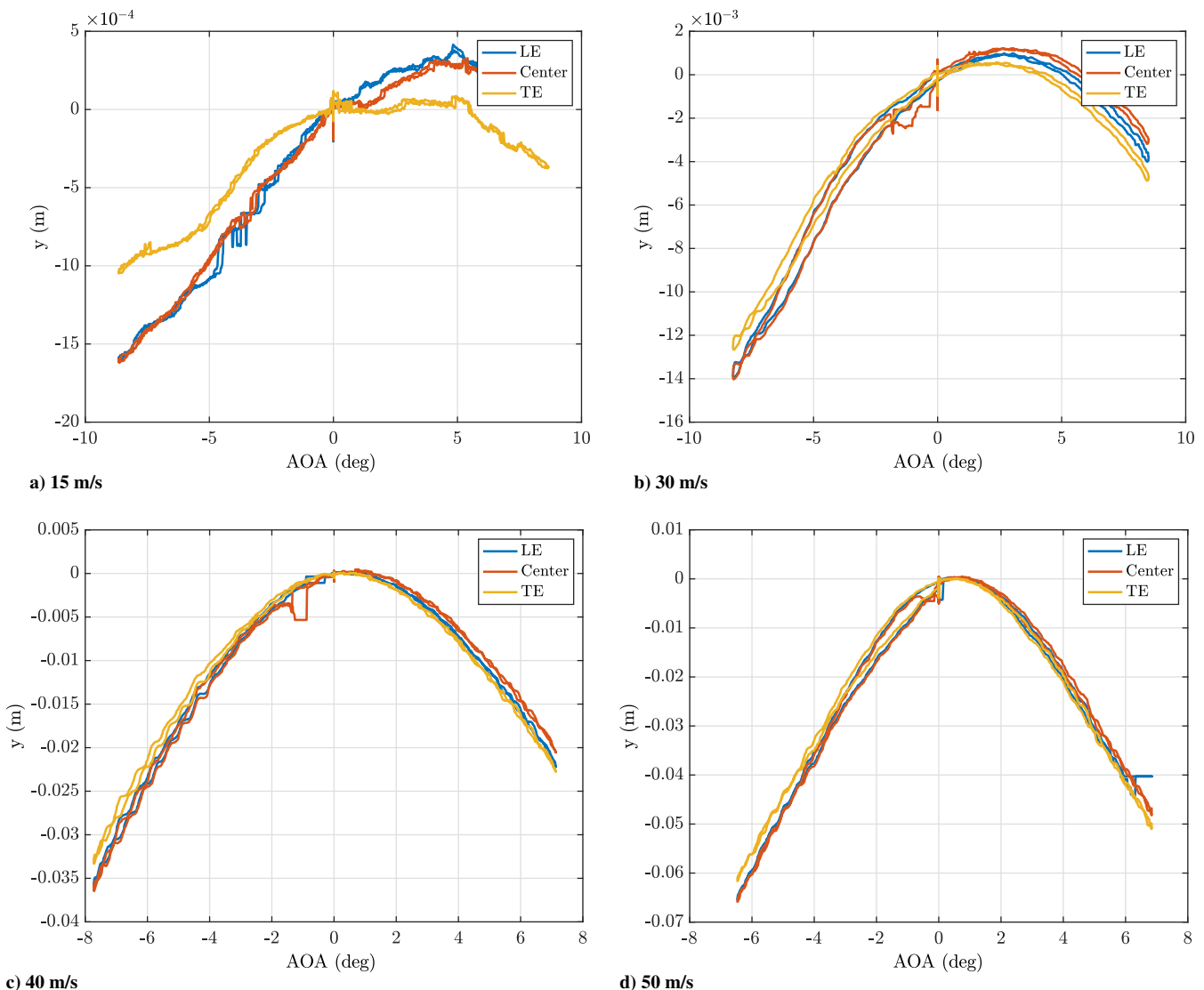


Fig. 23 Wing-tip spanwise deformations at the leading edge (LE), center chord (Center), and trailing edge (TE) during AOA sweeps; wind-tunnel test 1.

asterisks represent reflector locations in the undeformed (blue) and deformed (red) positions. Sensor positions along the leading and trailing edges, the centerline, and the wing-tip bar are connected for visualization. Figure 14 shows the corresponding first four strain modes, identified from strain data collected in the same excitation test. The asterisks mark the FBG sensor locations.

Finally, frequency data were also extracted for the wing installed in the wind tunnel to ensure that the wing clamping to the tunnel floor does not affect the structure's dynamics. The frequencies, reported in Table 6, were extracted from displacement and strain data for the test setup in which the wing was connected directly to the wind-tunnel floor (i.e., without the force balance). For comparison, Table 6 also shows the FE model frequencies.

B. Static Loading Test

Static loading tests were conducted on the wing with and without the Oralight skin, for model adaptation. In a pure bending test, the wing was loaded at the wing-tip center chord ($x = 50$ mm, $y = 558$ mm) with dead weights up to 3.0 and 2.0 kg for the skin-on and skin-off wings, respectively. In a coupled bending-torsion test, the weights were hung on the wing-tip rod, on the trailing-edge side, 80 and 40 mm behind the trailing edge for the skin-on and skin-off wings, respectively. The setup of the two tests is shown in Fig. 15. Also shown in Fig. 15 is a carbon rod weighing

15.5 g that was attached to the wing-tip rod to reinforce it against fracture.

Figures 16 and 17 show static loading results by means of wing-tip deflection and twist-angle versus load for the wing without and with the skin, respectively. Figures 16 and 17 compare the experimental results to Nastran linear analysis, for loads up to 2 kg. The computational results are for the adapted model, where both the Nylon 12 and Oralight skin Young moduli were significantly reduced from their nominal material properties (reported in Table 1). Without the skin, the model and test agree well in the linear range, for loads up to approximately 1 kg. For the skin-on wing, there are some discrepancies in the twist for the torsion load case. Because the Oralight skin properties are challenging to determine and vary significantly with tension (see Appendix B), no further model adaptations attempts were made. Figure 17 clearly shows the nonlinearity of the wing-twist response even for low loads.

It is noted that the experimental wing-tip displacement was estimated as the average of displacements at the leading and trailing edges, and the wing-tip twist angle was computed using the difference between the leading- and trailing-edge displacements and the distance between them [as $\arctan[(z_{LE} - z_{TE})/(x_{LE} - x_{TE})]$]. The subtraction of small quantities leads to values close to the order of the measurement error (order of 1 mm, which translates approximately up to 1.2 deg error). Therefore, some of the errors in Figs. 16c and 17c are attributed to measurement errors, and the model calibration therefore relied only

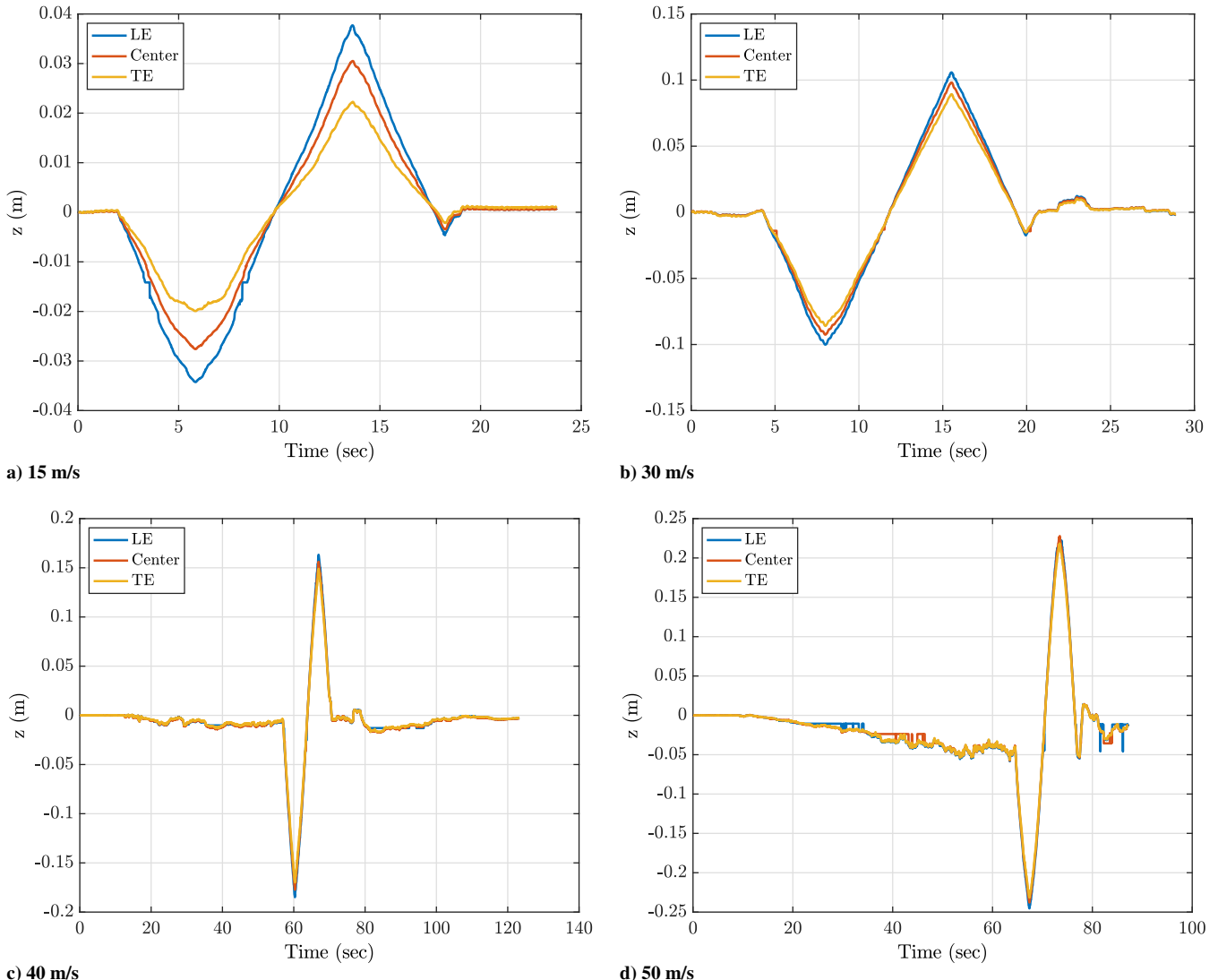


Fig. 24 Wing-tip normal deformations at the leading edge (LE), center chord (Center), and trailing edge (TE) during AOA sweeps; wind-tunnel test 1.

on the wing-tip deformation data. We also note that during the bending test of the wing with skin on localized yielding and wrinkling of the skin were observed, as also predicted (yield) by the stress analysis (Fig. 5).

V. Wind-Tunnel Experiments

Two wind-tunnel tests of the Pazy wing were conducted (the Pre-Pazy tests are briefly presented in Appendix A). In test 1, the wing was mounted on a force balance through a specially designed adapter (Fig. 18a). In test 2, the wing was mounted directly to the wind-tunnel floor using a 20 mm thick spacer plate (Fig. 18b). Test 1 served to extract static deformation data and corresponding aerodynamic data. The dynamic properties of the balance system interfered with those of the wing; thus, vibration response from this test was not indicative of the wing dynamic aeroelastic response. Test 2, with the wing mounted directly to the wind-tunnel floor, was used to record both the static and dynamic wing responses at the different test points. Test 2 was without any measurement of the aerodynamic loads.

Before these tests, a similar wing model, the Pre-Pazy wing, was tested in the wind tunnel. The Pre-Pazy wing was tested on the balance adapter at 0 deg root AOA and increasing airspeed, all the way to flutter failure. Measurements included wing-tip deformations only. This was a preliminary test for verification and validation of the manufacturing and experimental techniques that served as the

basis for the following tests of the Pazy wing. The Pre-Pazy model has similar topology and properties, but, due to manufacturing tolerances and instrumentation, it is not the same as the Pazy wing. The Pre-Pazy wing and some of its test results are detailed in Appendix A.

In test 1, root AOA sweeps were performed at fixed airspeeds of 15, 30, 40, and 50 m/s, and velocity sweeps were performed at 3, 5, and 7 deg root AOA. In test 2, velocity sweeps were conducted at 5, -5, and 7 deg root AOA. Results are presented separately for tests 1 and 2 because, as noted previously, the different mounts affected the wing's dynamic response (but not the static response). Specifically, we observed that in test 1 the wing was at a static position (i.e., did not vibrate) at airspeeds above the estimated flutter speed due to the dynamic interference of the balance adapter.

In both tests, a 10 g weight was attached to the wing-tip rod to delay the flutter onset (as discussed in Sec. III.B). In test 1, the weight was connected 40 mm behind the trailing edge, as shown in Fig. 19, and in test 2, the weight was connected at the trailing edge.

A. Wind-Tunnel Test 1

1. AOA Sweep

Four root AOA sweeps were carried out, at fixed airspeeds of 15, 30, 40, and 50 m/s. The wind-tunnel airspeed was first increased to the desired speed, after which the turntable rotated the wing, first to the negative and then to the positive required maximal root

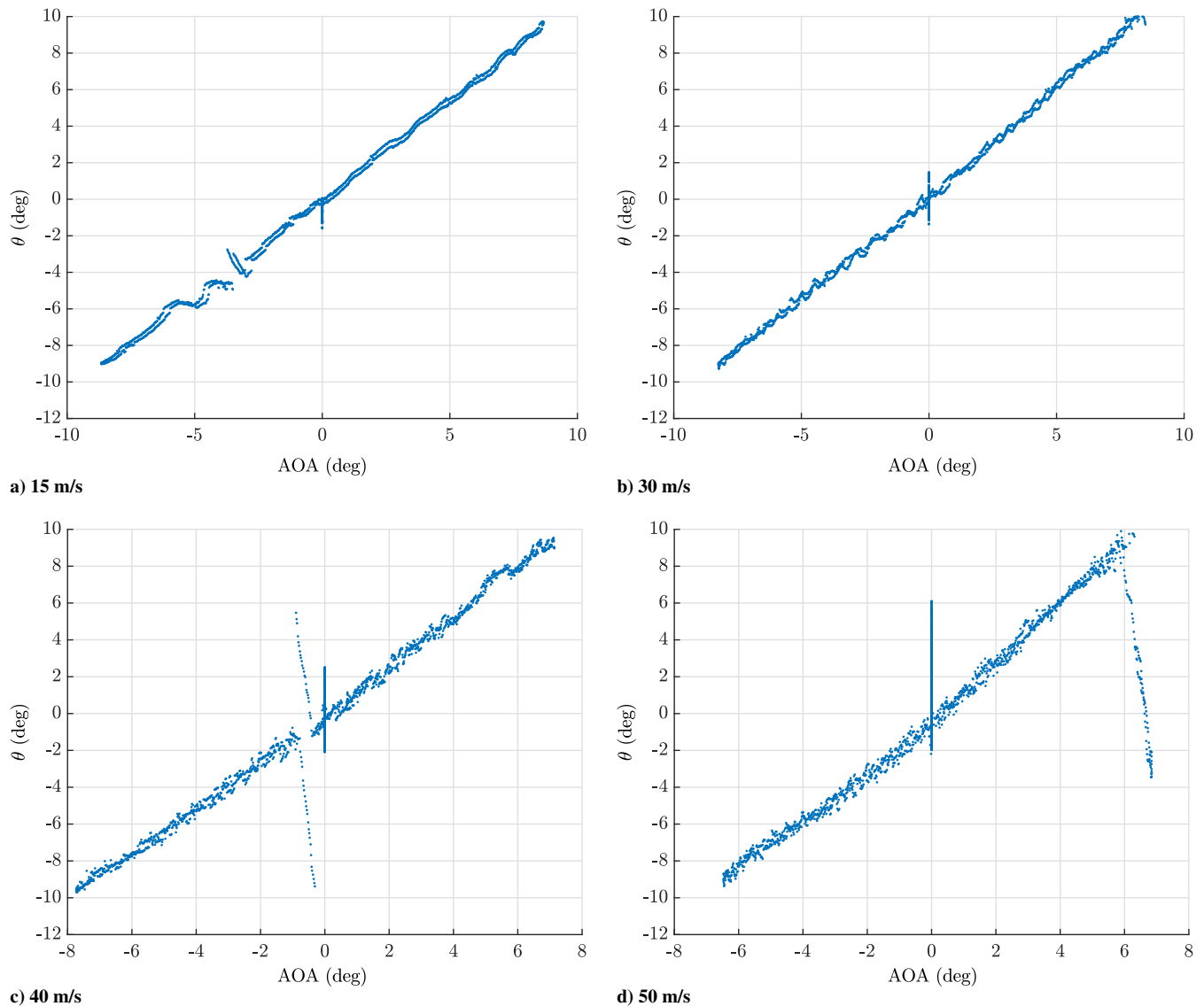


Fig. 25 Wing-tip local AOA (rigid AOA plus elastic twist angle) during AOA sweeps; wind-tunnel test 1.

AOA, then returned it to zero. The airspeed was measured via a pitot tube, and the aerodynamic loads were recorded by the five-degrees-of-freedom force balance at 1 kHz. Displacements were measured by the MRS at 120 Hz, and strains were measured by the FOS at 1 kHz.

We note that the wing, without any forces acting on it, is not perfectly straight. Figure 20 shows the wing's initial state as captured by the MRS sensors (in red) compared to a theoretically straight, flat wing (blue). The leading and trailing edges are deflected by -22.5 and -20.9 mm, respectively, resulting in a negative twist angle of approximately 1° . As a result, it was impossible to perfectly calibrate the turn table. All the results below show incremental values. Asymmetry in response to negative and positive root AOA values can be attributed to the initial twist. Moreover, MRS measurements were performed through the wind-tunnel window, which made the MRS calibration process more difficult and most likely affected the MRS accuracy.

Figure 21 shows the wing-tip leading-edge, center, and trailing-edge incremental out-of-plane displacements versus root AOA, presenting the nonlinear response at the large AOA and dynamic pressure values. Figures 22 and 23 show the wing-tip incremental chordwise and spanwise deformations. In all three directions, there is asymmetry between the positive and negative root AOA response. Figure 24 shows the wing-tip displacements versus time during these AOA sweeps, including the times at which the root

AOA was ramped up and down. We note that at 40 and 50 m/s there is an initial incremental tip deformation of approximately 10 and 50 mm, respectively, even for zero root AOA (before the AOA sweep starts). This is likely due to the initial twist of the wing creating an aerodynamic force that is amplified at the large dynamic pressures.

Figure 25 shows the wing-tip local AOA (rigid AOA plus elastic deformation) during the AOA sweeps, computed from the difference between the leading- and trailing-edge incremental displacements. The following gives a few observations and comments that may be useful if the data are used for model validation:

- 1) The wing-tip angles in Fig. 25 do not include the -1° twist built in the model (Fig. 20).

- 2) Some spikes are observed in times when the MRS lost track of reflectors.

- 3) Because of wing vibrations, there are fluctuations in the wing-tip angles, shown in Fig. 26. These fluctuations are larger at the higher airspeeds. They are in the order of magnitude of the elastic twist, thus making it difficult to get a reliable estimation of the twist angle.

Tables 7 and 8 summarize the max wing-tip center-chord deformation (x : chordwise; y : spanwise; z : normal) and twist angle measured at each test at the maximal positive and negative root AOA. As noted, the twist angle estimation is subject to several error sources.

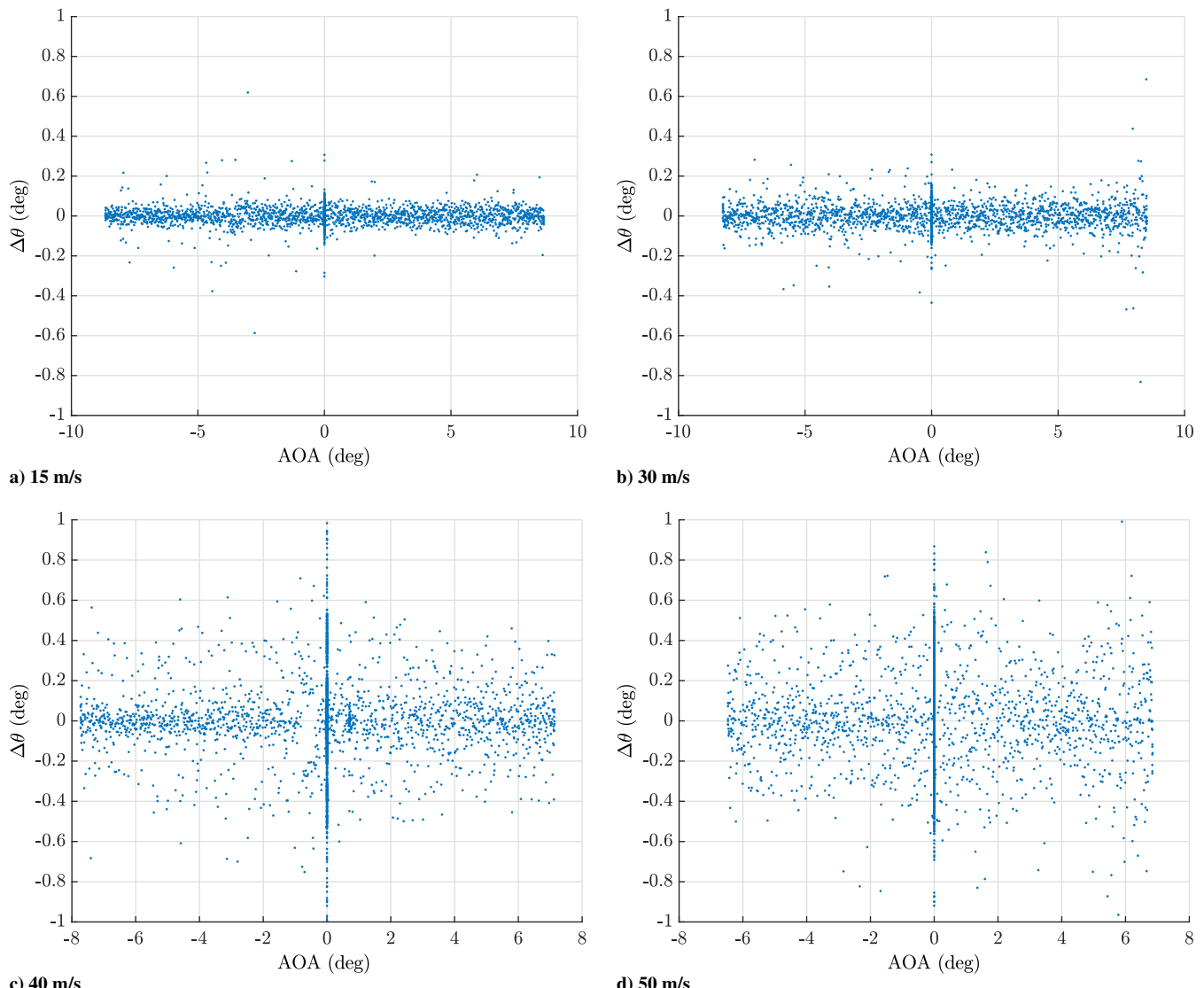


Fig. 26 Wing-tip local AOA fluctuations during AOA sweeps; wind-tunnel test 1.

Table 7 AOA sweep: wing-tip midchord deformations and twist angle at maximum negative AOA

V , m/s	q_D , Pa	AOA, deg	z deformation (mm), (% span)	x deformation (mm), (% span)	y deformation (mm), (% span)	θ , deg
15	137	-8.4	-27.6 (5.0)	5.5 (1.0)	-1.6 (0.3)	-0.4
30	518	-8.2	-92.6 (16.8)	15.4 (2.8)	-14.0 (2.6)	-0.5
40	982	-7.7	-177.0 (32.2)	21.8 (4.0)	-36.5 (6.6)	-1.4
50	1516	-6.5	-237.5 (43.3)	25.7 (4.7)	-65.9 (12.0)	-1.9

Table 8 AOA sweep: wing-tip midchord deformations and twist angle at maximum AOA

V , m/s	q_D , Pa	AOA, deg	z deformation (mm), (% span)	x deformation (mm), (% span)	y deformation (mm), (% span)	θ , deg
15	137	8.5	30.5 (5.5)	3.0 (0.5)	—(—)	0.7
30	518	8.5	98.1 (17.8)	12.6 (2.3)	-3.1 (0.6)	1.5
40	982	7.1	156.4 (28.4)	23.0 (4.2)	-20.5 (3.7)	1.9
50	1516	6.8	228.4 (41.5)	33.1 (6.0)	-48.2 (8.8)	—

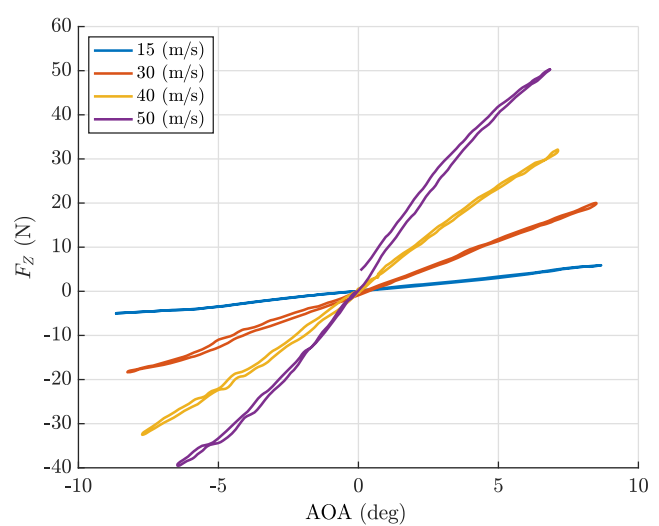


Fig. 27 Normal force vs AOA; wind-tunnel test 1.

Figure 27 presents the normal force as a function of root AOA measured in these tests, showing a reduction of the slope of the force at large deformation conditions. Some hysteresis in the force

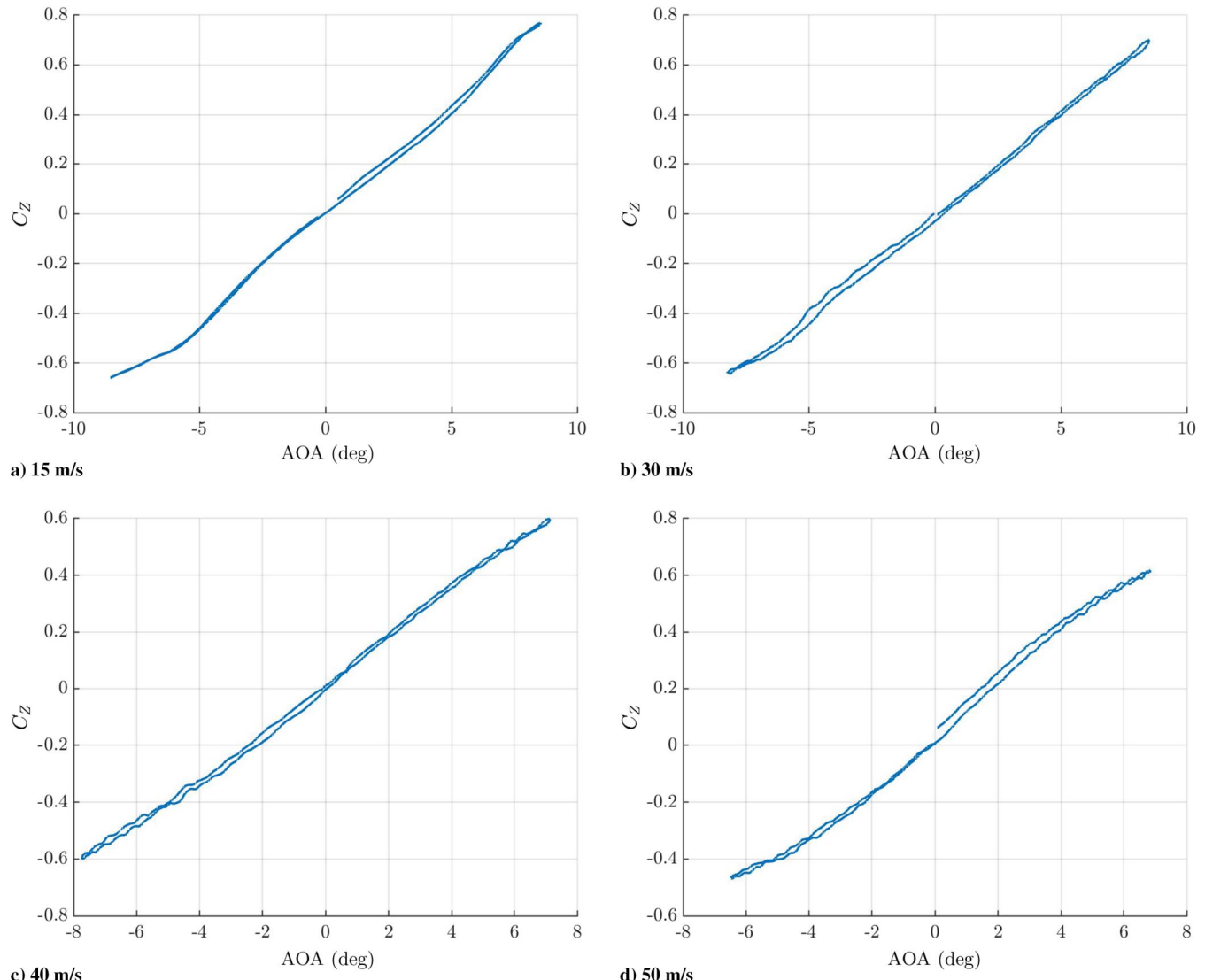


Fig. 28 Normal force coefficients vs AOA; wind-tunnel test 1.

Table 9 AOA sweeps first-order regression polynomials: $C_z = C_1\alpha + C_0$, α in degrees

Coefficient	15 m/s	30 m/s	40 m/s	50 m/s
C_0	0.00044	0.019	0.0061	0.027
C_1	0.086	0.082	0.083	0.088

Table 10 AOA sweeps second-order regression polynomials: $C_z = C_2\alpha^2 + C_1\alpha + C_0$, α in degrees

Coefficient	15 m/s	30 m/s	40 m/s	50 m/s
C_0	0.018	0.028	0.0049	0.014
C_1	0.086	0.082	0.084	0.088
C_2	0.00072	0.00038	0.00058	0.00087

measurement is noted. Figure 28 shows the normal force coefficient for each case. Tables 9 and 10 show the first- and second-order regression polynomials, respectively, of the normal force coefficient. The positive and negative branches of the normal force coefficient curves are not exactly symmetric, likely due to the initial wing twist. At the lowest airspeed of 15 m/s (Fig. 28a), the curve slope is not constant even for small root AOA. This could be attributed to the low

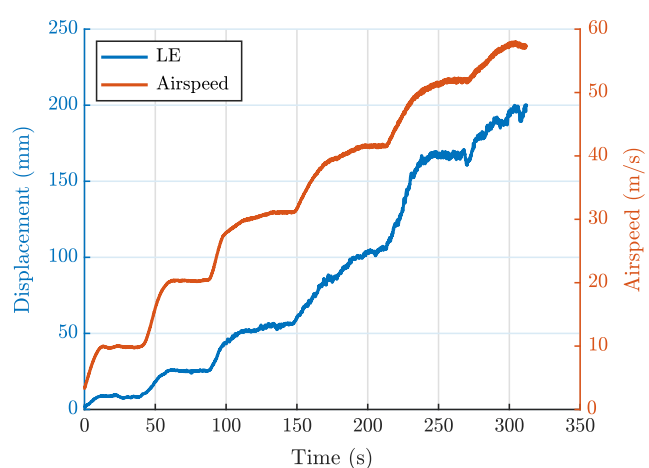


Fig. 29 An example of velocity and wing-tip leading-edge (LE) deflection change in time as recorded in a velocity sweep at 5 deg AOA; test 1.

Reynolds number of the test ($Re \approx 10^5$). At the highest airspeed of 50 m/s ($Re \approx 3.2 \times 10^5$), there is a distinct reduction in the normal force coefficient at the large root AOA for which the wing deformations are large.

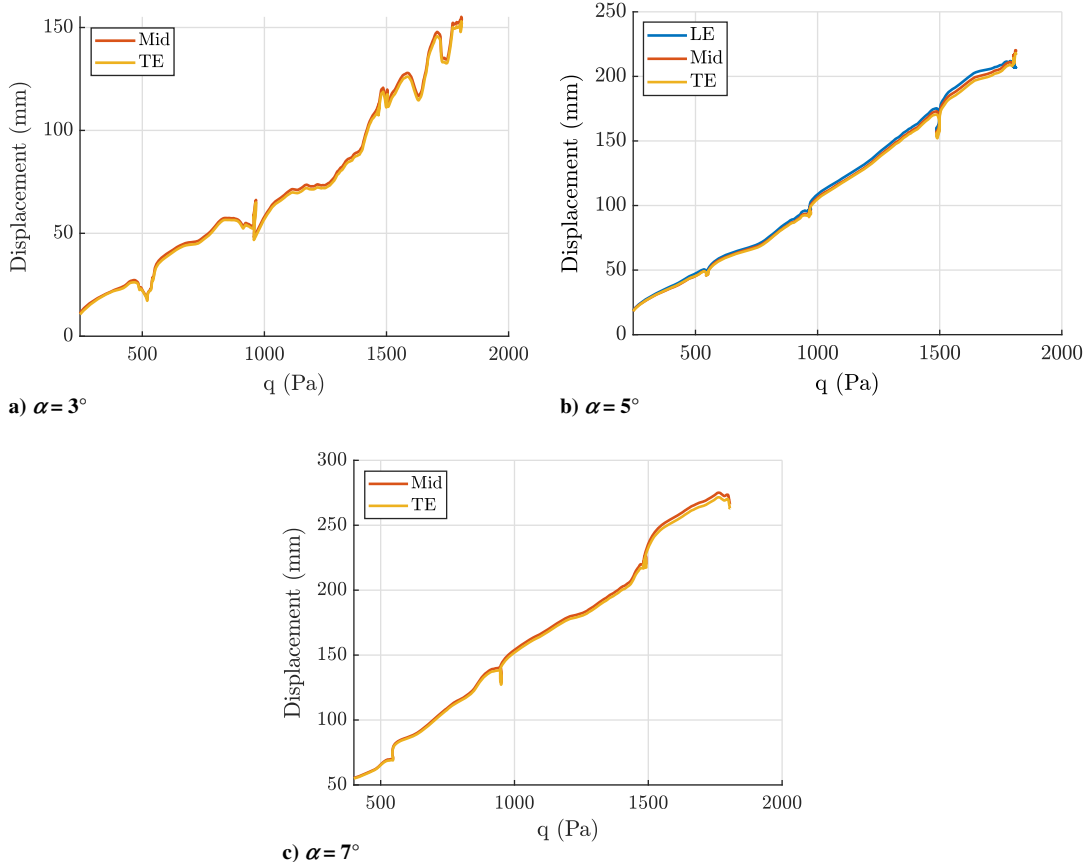


Fig. 30 Displacement trends at the wing tip vs dynamic pressure at different AOA values; test 1.

Table 11 Maximal wing-tip deformation in velocity sweeps; test 1

AOA, deg	V, m/s	q_D , Pa	LE, mm (% span)	Center, mm (% span)	TE, mm (% span)
3	56.7	1806	— —	155 (28)	153 (27)
5	56.0	1763	211 (38)	211 (38)	206 (37)
7	56.0	1763	— —	275 (50)	271 (49)

2. Velocity Sweep

Several velocity sweeps were carried out, in which the wing was kept at a fixed root AOA and the velocity was gradually increased. At increments of 10 m/s (or 5 m/s, where needed), the velocity was held constant for a period of approximately 15 s for data collection. It is noted that the wind-tunnel operates in open loop and the airspeed is controlled via a potentiometer. Therefore, "keeping the airspeed fixed" only means keeping a fixed velocity input command. As an example of a velocity sweep test, Fig. 29 shows the velocity and wing-tip displacement during the time duration of a velocity sweep at 5 deg root AOA. Displacements were measured by the MRS at 120 Hz, and strains were measured by the FBG sensors at 1 kHz.

Figure 30 shows wing-tip displacement data from three velocity sweeps in which the airspeed was increased to approximately 56 m/s. Both the MRS and wind-tunnel data were smoothed to remove fluctuations, such that the plots reflect the trend of deflection versus the dynamic pressure. Smoothing was done using convolution with a moving average of 500 samples. For the 7 deg AOA case, the standard deviation of the normalized airspeed (measured airspeed divided by the smoothed airspeed) is 0.03, and the standard deviation of the normalized center-chord displacement is 0.01. The spikes and



Fig. 31 Deformed wing at 7 deg AOA and 55 m/s; test 1.

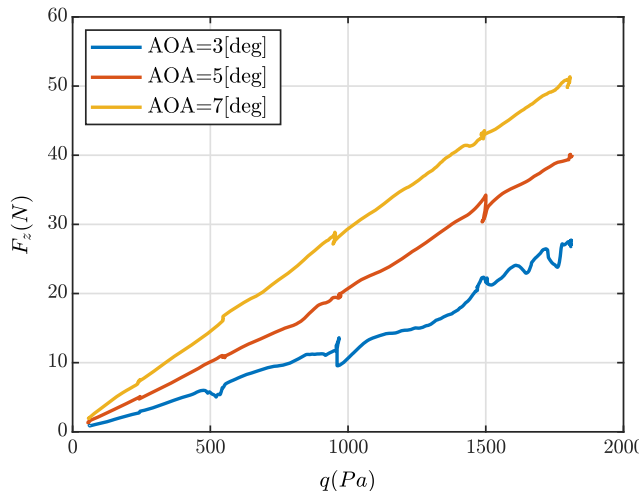


Fig. 32 Normal force vs dynamic pressure at the various AOA values; velocity sweeps, test 1.

Table 12 GVT data for the wing with a 10 g trailing-edge weight, measured in the wind tunnel

Mode	Frequency, Hz	Frequency, Hz
Data (method)	Disp. (SPOD)	Strains (SPOD)
First bending	4.2	4.0
Second bending	27.6	27.5
First torsion	39.0	38.0
Fore-aft bending with torsion	—	65.3
Third bending	—	80.2

nonsmooth behavior of the deformation with dynamic pressure can be attributed to fluctuations of the airspeed that are not adequately measured (or measured with a delay), wing vibrations, and measurement errors of the MRS. However, they provide the trends of deformation variation. Table 11 summarizes the wing-tip deformations at the highest tested airspeeds for each root AOA. At the extremest aerodynamic load, wing-tip deformations of 50% span were recorded (Fig. 31).

Figure 32 shows the normal force that was measured at the three velocity sweeps. These trends represent the change in the normal force due to the dynamic pressure, the elastic wing twist and deformation, and also variation of the Reynolds number (approximately between $Re \approx 5 \times 10^4$ at 10 m/s to $Re \approx 3.2 \times 10^5$ at 50 m/s).

B. Wind-Tunnel Test 2

In this test, the wing was connected to the wind-tunnel floor directly via a thin connector plate (i.e., this test was done without force balance). A 10 g weight was attached to the wing-tip trailing edge to delay flutter onset. Measurements included the wing deformations via the MRS and strains from the FBG FOS.

A GVT of the wing, with the 10 g trailing-edge weight, was performed while the wing was installed in the wind tunnel.

Table 13 Maximal wing-tip deformation in velocity sweeps; test 2

AOA, deg	V, m/s	q_D , Pa	LE, mm (% span)	Center, mm (% span)	TE, mm (% span)
-5	57.0	1838	220 (40)	218 (39)	217 (39)
5	56.0	1853	195 (35)	191 (34)	191 (34)
7	43.0	1050	160 (29)	155 (28)	155 (28)

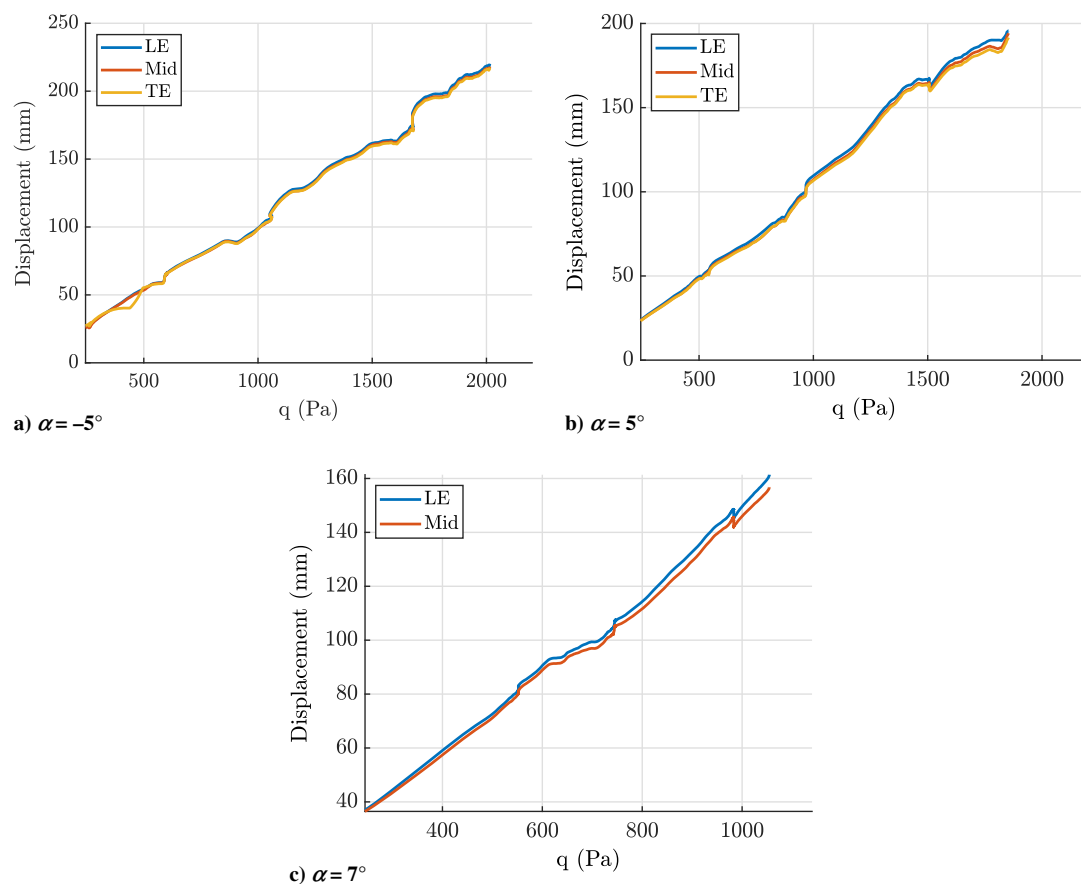


Fig. 33 Displacement trends at the wing tip vs dynamic pressure at different AOA values; test 2.

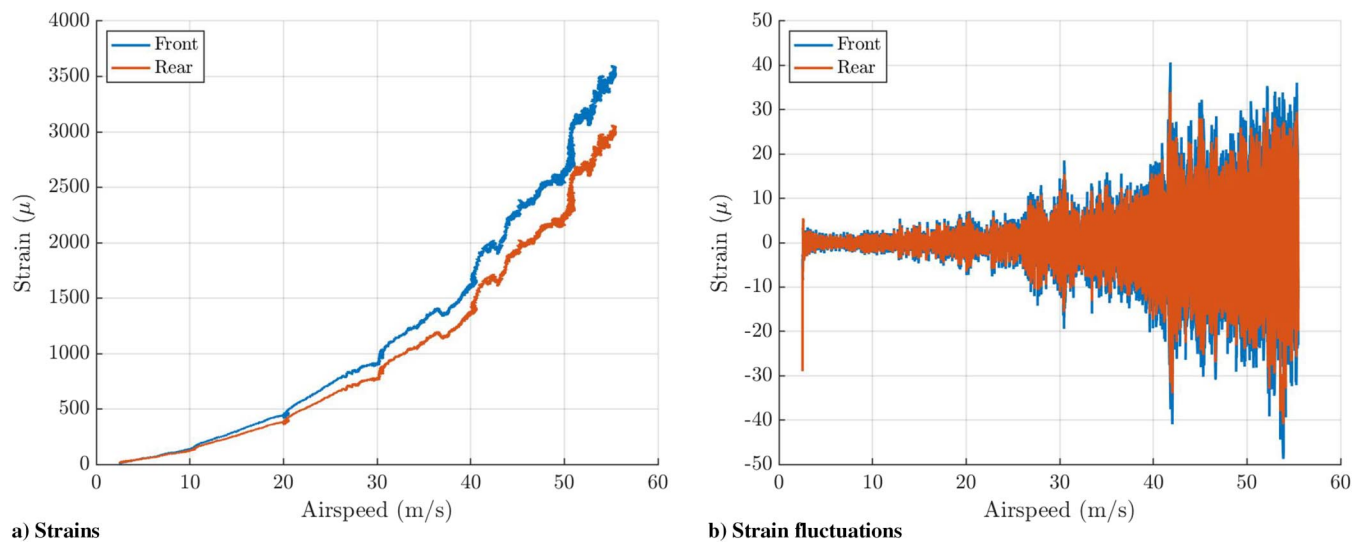


Fig. 34 a) Strains and b) strain fluctuations at the wing root vs airspeed at -5 deg AOA; velocity sweep, test 2.

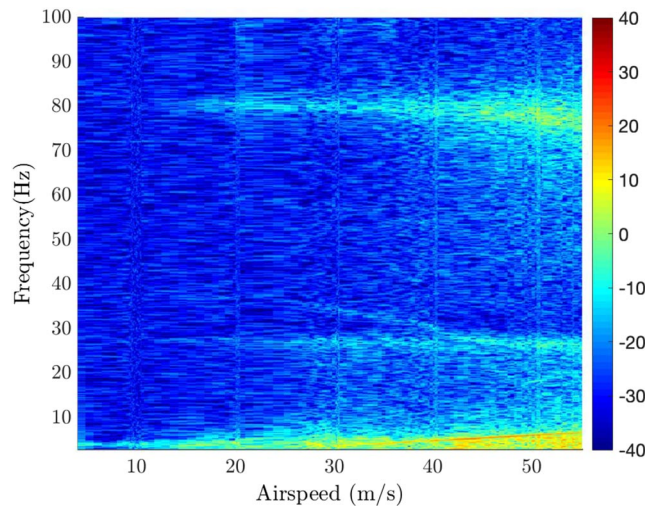


Fig. 35 Aeroelastic frequencies vs airspeed at -5 deg AOA; velocity sweep, test 2.

Table 12 reports the measured frequencies. The frequencies agree well with those from free-vibration analysis with the added weight. It is noted that because the MRS in the wind tunnel has a sampling frequency of 120 Hz modes above 60 Hz could not be identified.

Velocity sweeps were performed for root AOA of -5 , 5 , and 7 deg. Figure 33 shows wing-tip deformations versus dynamic pressure, and Table 13 presents the maximal wing-tip deformations that were recorded. At 5 deg root AOA, the deformations are within 3% of those measured at similar conditions in test 1 (Table 11), thus confirming that the experiment is repeatable and that the balance adapter did not have an effect on the static deformation.

1. -5 deg AOA Velocity Sweep

Figure 34 shows the strains and strain fluctuations versus airspeed. The maximal measured strain level is 3600μ , found at the root of the front side of the aluminum spar. Strain fluctuations steadily increase with airspeed. There appears to be a peak strain response at about 43 m/s, which disappears with airspeed increase, that may indicate an instability at that speed. We recall

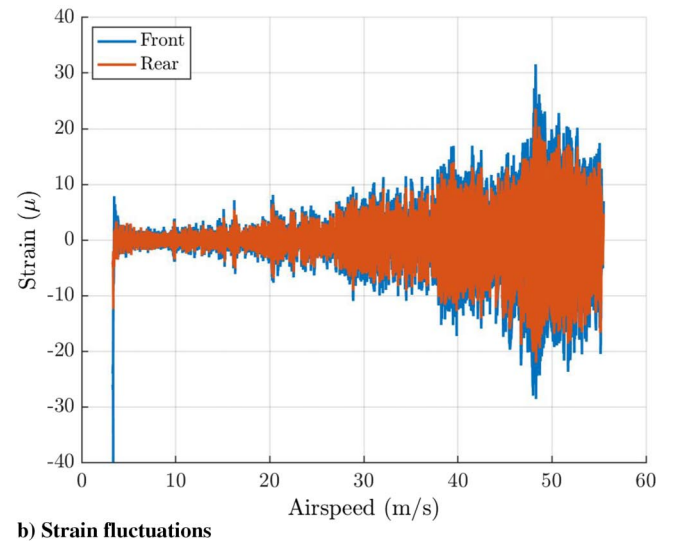
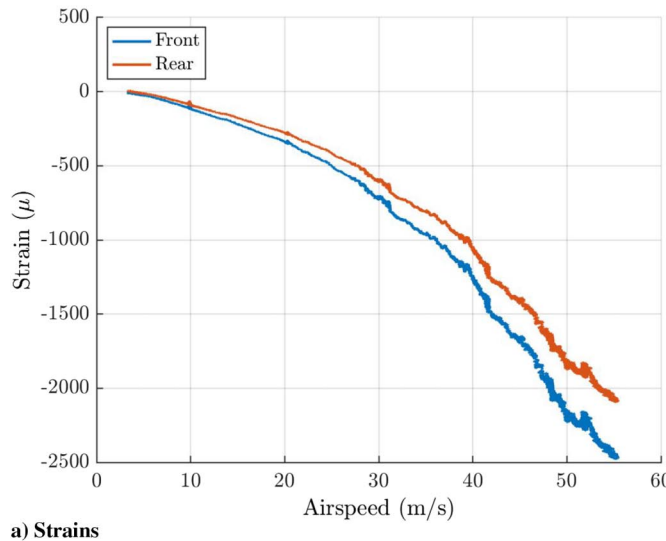


Fig. 36 a) Strains and b) strain fluctuations at the wing root vs airspeed at 5 deg AOA; velocity sweep, test 2.

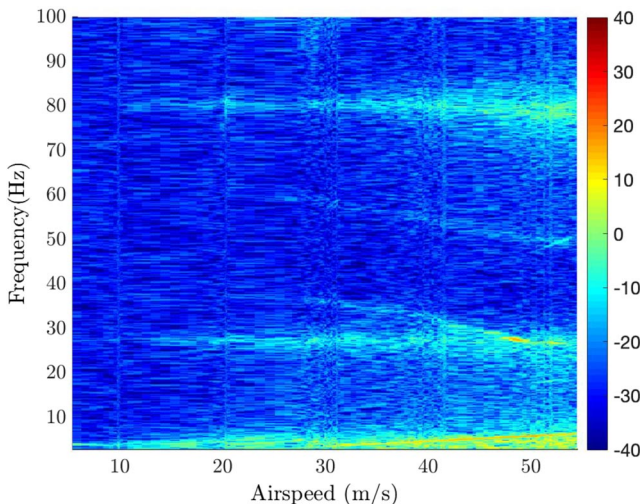


Fig. 37 Aeroelastic frequencies versus airspeed at 5 deg AOA; velocity sweep, test 2; warm colors denote larger amplification.

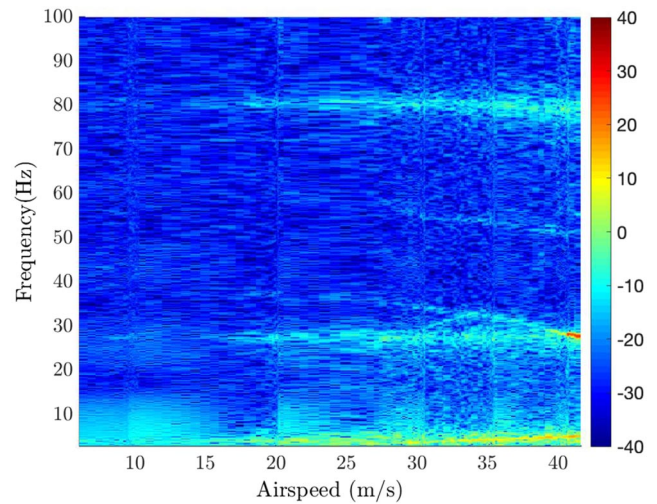


Fig. 40 Aeroelastic frequencies vs airspeed at 7 deg AOA; velocity sweep, test 2; warm colors denote larger amplification.

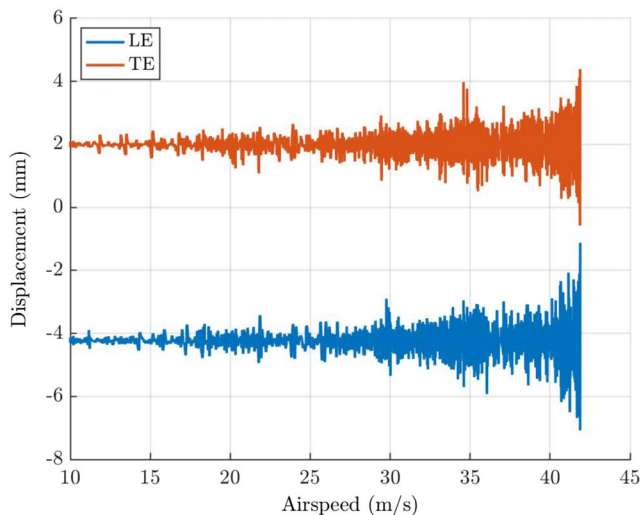
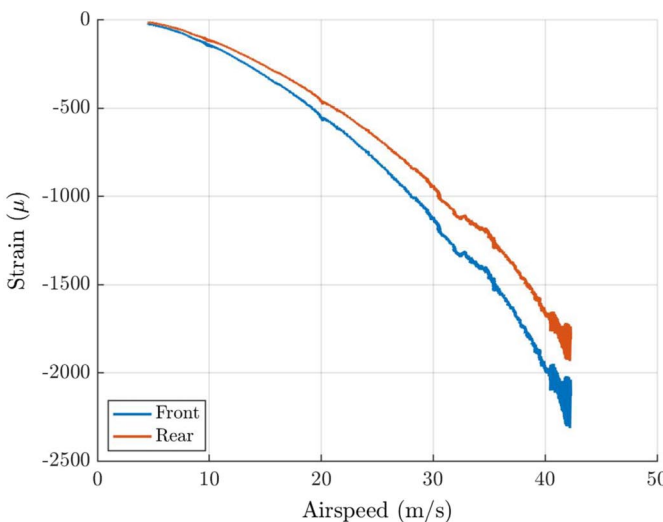


Fig. 38 Displacements fluctuations at the wing tip vs airspeed at 7 deg AOA; velocity sweep, test 2.

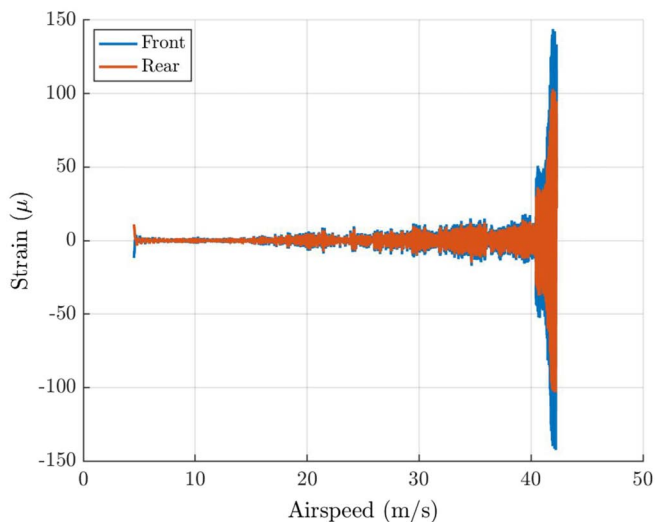
that the airspeed was steadily increased from 40 to 50 m/s, so it is likely that an instability region was present at 42 m/s and passed through, after which the system was again stable. Figure 35 shows a spectrogram of the aeroelastic frequencies versus airspeed, as computed from the data of a single FBG sensor. The frequencies time histories were computed using short-term Fourier transform, by dividing the data into 100 segments with 80% overlap. The spectrogram shows the decrease of the first torsion mode frequency (starting at 38 Hz at zero velocity) and its coalescence with the second bending mode (starting at 27.5 Hz at zero velocity), which supports the possibility of instability at 43 m/s. As the airspeed increases, the torsion mode frequency becomes lower than the second bending, explaining the regained stability of the system at the higher airspeeds. A similar phenomenon was captured for a 5 deg root AOA velocity sweep, shown and discussed next.

2. 5 Deg AOA Velocity Sweep

Wing-tip deformations versus airspeed are shown in Fig. 33b. The deformations are close to those of -5° deg root AOA, but the cases are not exactly symmetric. At the maximal dynamic pressure of 1853 Pa,



a) Strains



b) Strain fluctuations

Fig. 39 a) Strains and b) strain fluctuations at the wing root vs airspeed at 7 deg AOA; velocity sweep, test 2.

the wing-tip displacements were about 5% less than in the -5° deg root AOA case. This is likely due to the initial wing twist (Fig. 20). Figure 36 shows the strains and strain fluctuations versus airspeed. The maximal measured strain level is approximately $-2500 \mu\text{s}$, at the root of the front side of the aluminum spar. Strain fluctuations steadily increase with airspeed. Also in this case, there is peak strain response, at 48 m/s, which disappears when the airspeed is increased. The spectrogram in Fig. 37 shows frequencies coalescence at 48 m/s, supporting the possibility of instability.

3. 7 Deg AOA Velocity Sweep

In the 7 deg root AOA velocity sweep, the airspeed was increased from 0 to 42 m/s (dynamic pressure of 1050 Pa). At 43 m/s, large second bending oscillations were visible, and the wind-tunnel velocity was rapidly (manually) reduced. Wing-tip deformations versus airspeed are shown in Fig. 33c, and wing-tip displacement fluctuations are shown in Fig. 38.

Figure 39 shows the strains and strain fluctuations versus airspeed. The maximal measured strain level is approximately $-2300 \mu\text{s}$ at the aluminum spar's root front side. Strain fluctuations growth indicate instability at 40 m/s. The spectrogram in Fig. 40 shows a reduction of the torsion frequency with airspeed, frequency coalescence of the torsion and second-bending modes, and amplification of the response at this speed. We note that in all three velocity sweeps (at 5, -5 , and 7 deg root AOA), Limit Cycle Oscillations (LCO) started when the wing had approximately the same deformed shape, with wing-tip deformation of about 25% wingspan. It was also shown numerically in Ref. [19] that at about 20% wing-tip deformation (independent of the exact combination of root AOA and dynamic pressure) there is a rapid decrease in the flutter onset speed, explaining the observed instabilities.

VI. Conclusions

The paper presented the design, analysis, and test results of the Pazy wing, a wind-tunnel benchmark of a very flexible wing. Linear and nonlinear static and dynamic aeroelastic analyses were used to design the experimental campaign. Two wind-tunnel tests were conducted, during which the wing's deformations, strains, and aerodynamic coefficients were measured. In the first wind-tunnel test, velocity and root AOA sweeps were performed in which the wing-tip deformations were up to 50% span. In this test, the wing was mounted on a force balance, such that aerodynamic forces were measured. In the second wind-tunnel test, the wing was mounted directly to the tunnel's floor (i.e., without the force balance). LCO was encountered during velocity sweeps at several AOA values when the wing-tip deformation was approximately 25% of the span. Large data sets of deformations and strains were collected via a motion recovery optical system and with optical-fibers Bragg sensors, respectively. All the data and the Pazy wing models are publicly available through the 3rd Aeroelastic Prediction Workshop.¹¹ This large data set can hopefully serve in future studies validating computational models of very large deformations and studying various aspects of the aeroelastic response of flexible wings.

Appendix A: Pre-Pazy Wing: Dynamic Properties and Test Results

Table A1 presents the first structural frequencies as measured in GVT and from the adapted FE model.

The Pre-Pazy wing was tested with a 10 g weight attached to the wing-tip loading rod at the trailing edge. Only the wing-tip deformations were measured ($x = 0, 100 \text{ mm}, y = 550 \text{ mm}$). Table A2 presents tip deformation and twist angle at different test conditions. Figure A1 shows the deformed wing at 7 deg root AOA, 55 m/s.

¹¹Data available online at <https://nescacademy.nasa.gov/workshops/AePW3/public>.

Table A1 Pre-Pazy wing frequencies

Mode	GVT, Hz	FEM, Hz
First bending	4.6	4.7
Second bending	29.5	30.6
First torsion	42.6	42.2

Table A2 Pre-Pazy wing-tip center-chord deformation at static loading conditions: experimental data

	AOA, deg	V, m/s	q_D , Pa	Tip deformation, mm	θ , deg
Linear, small deformation	5	30	543	52 (9% span)	0.74
Large deformation small AOA	5	50	1469	157 (28% span)	2.3
Very large deformation	7	55	1830	255 (46% span)	3.5

Exp: 12624 Time: 3528 AL1: 6.99 AIR SPEED (m/sec): 55.32



Fig. A1 Photo of the deformed Pre-Pazy wing at 7 deg AOA and 55 m/s airspeed.

The wing was tested for flutter at 0 deg root AOA, without the trailing-edge weight. Linear stability analysis predicted flutter at 61 m/s (Fig. A2). Nonlinear flutter analyses of the Pre-Pazy wing are presented in Refs. [19,23]. In the test, the wing fluttered at 70 m/s. After the test, it was discovered that the balance mount introduced its own dynamics to the system. Thus, the collected dynamic data of the Pre-Pazy wing, including flutter onset speed, are not representative of the wing's dynamics.

Appendix B: Tensile Test to Determine Mechanical Properties of Oralight Skin

The modulus of elasticity of the polyester Oralight wing cover was determined in a tensile test (Fig. B1a). The results also served for a severe approximation for the ultimate strain. The test was conducted on a rectangular 120 mm by 50 mm specimen that was folded four times to allow larger forces and better accuracy. The results of the tests are presented in Fig. B1b in terms of engineering and true stress and strain. The results are given in terms of stress that is defined as the force per unit width (and not area). For thin sheets, this formulation is more consistent because the thickness is hard to measure. For the simulations, the thickness of the Oralight is assumed, based on the manufacturer's data sheet, as 12 μm . The

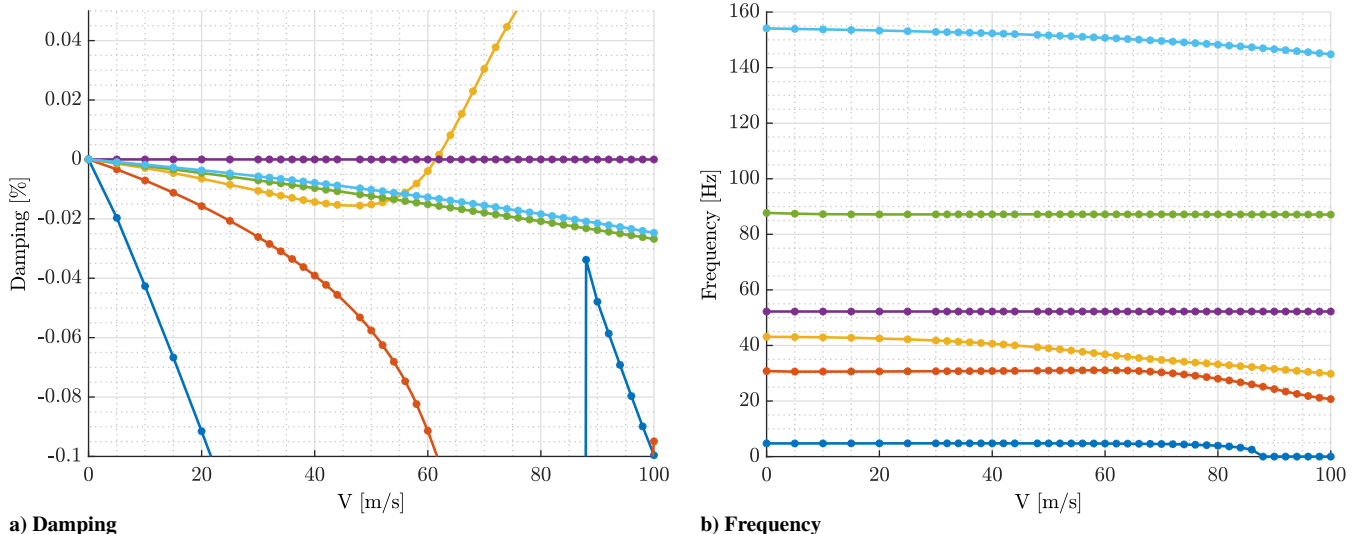
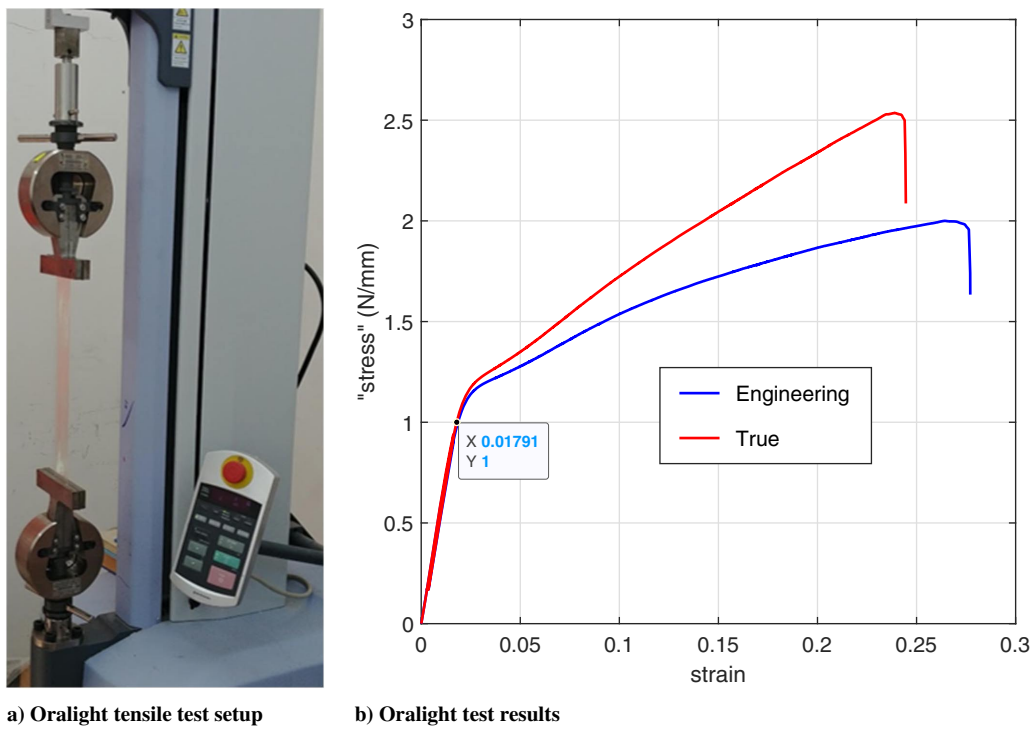
Fig. A2 ω – V – g plot, Pre-Pazy wing, without weight; 0 deg AOA.

Fig. B1 Oralight tensile test.

results are then translated into actual stress. It is noted that the thickness of the foil has no effect on the results as long as the stiffness per unit width is consistent because the bending stiffness of the foil is negligible. The ultimate strain assumes uniform strain over the foil and neglects necking and local stress concentration near the clamping regions. The actual local strain in the region of failure would be higher.

Acknowledgement

The authors would like to gratefully acknowledge the support of the Pazy Foundation in this research project.

References

- [1] Noll, T. E., Brown, J. M., Perez-Davis, M. E., Ishmael, S. D., Tiffany, G. C., and Gaier, M., "Investigation of the Helios Prototype Aircraft Mishap Volume I Mishap Report," Vol. 9, 2004, p. 2004.
- [2] Xiang, J., Yan, Y., and Li, D., "Recent Advance in Nonlinear Aeroelastic Analysis and Control of the Aircraft," *Chinese Journal of Aeronautics*, Vol. 27, No. 1, 2014, pp. 12–22.
- [3] Su, W., and Cesnik, C. E. S., "Dynamic Response of Highly Flexible Flying Wings," *AIAA Journal*, Vol. 49, No. 2, 2011, pp. 324–339.
- [4] Cea, A., and Palacios, R., "Nonlinear Modal Aeroelastic Analysis from Large Industrial-Scale Models," *AIAA Scitech 2019 Forum*, AIAA, Reston, VA, 2019, pp. 2–12.
- [5] Ritter, M., and Cesnik, C. E., "An Enhanced Modal Approach for Large Deformation Modeling of Wing-Like Structures," *AIAA SciTech*, AIAA, Reston, VA, 2015, pp. 1–16.
<https://doi.org/10.2514/6.2015-0176>
- [6] Bernhammer, L. O., Breuker, R. D., and Karpel, M., "Geometrically Nonlinear Structural Modal Analysis Using Fictitious Masses," *AIAA Journal*, Vol. 55, No. 10, 2017, pp. 3584–3593.
<https://doi.org/10.2514/1.J054787>
- [7] Kantor, E., Raveh, D. E., and Cavallaro, R., "Nonlinear-Structural-Nonlinear-Aerodynamic Model for Static Aeroelastic Problems," *AIAA*

- Journal*, Vol. 57, No. 5, 2019, pp. 2158–2170.
<https://doi.org/10.2514/1.J057309>
- [8] Drachinsky, A., and Raveh, D. E., “Modal Rotations: A Modal-Based Method for Large Structural Deformations,” *AIAA Journal*, Vol. 58, No. 7, 2020, pp. 3159–3173.
<https://doi.org/10.2514/1.J058899>
- [9] Tang, D., and Dowell, E. H., “Experimental and Theoretical Study on Aeroelastic Response of High-Aspect-Ratio Wings,” *AIAA Journal*, Vol. 39, No. 8, 2001, pp. 1430–1441.
- [10] Britt, R. T., Ortega, D., McTigue, J., and Scott, M. J., “Wind Tunnel Test of a Very Flexible Aircraft Wing,” *AIAA/ASME/ASCE/AHS/ASC Structures, Structural Dynamics and Materials Conference*, AIAA, Reston, VA, 2012, pp. 1–0.
- [11] Cooper, J. E., Cook, R. G., Francois, G., Óscar de la Torre, Rodríguez, Neild, S. A., Lowenberg, M. H., Alexander, S., Coetzee, E., and Evans, M., “Wind Tunnel Testing of a High Aspect Ratio Wing Model,” *Proceedings of the International Forum on Aeroelasticity and Structural Dynamics*, 2019, pp. 094–1.
- [12] Richards, L., Parker, A. R., Ko, W. L., and Piazza, A., “Fiber Optic Wing Shape Sensing on NASA’s Ikhana UAV,” *Proceedings of the NAVAIR Meeting*, Edwards, CA, Vol. 7, 2008.
- [13] Nicolas, M. J., Sullivan, R. W., and Richards, W. L., “Large Scale Applications Using FBG Sensors: Determination of In-Flight Loads and Shape of a Composite Aircraft Wing,” *Aerospace*, Vol. 3, No. 3, 2016, p. 18.
- [14] Roessler, C., Stahl, P., Sendner, F., Hermanutz, A., Koeberle, S., Bartashevicius, J., Rozov, V., Breitsamter, C., Hornung, M., Meddaikar, Y. M., Dillinger, J., Sodja, J., De Breuker, R., Koimtzoglou, C., Kotinis, D., and Georgopoulos, P., “Aircraft Design and Testing of FLEXOP Unmanned Flying Demonstrator to Test Load Alleviation and Flutter Suppression of High Aspect Ratio Flexible Wings,” *AIAA Scitech 2019 Forum*, AIAA Paper 2019-1813, 2019.
- [15] Gherlone, M., Cerracchio, P., and Mattone, M., “Shape Sensing Methods: Review and Experimental Comparison on a Wing-Shaped Plate,” *Progress in Aerospace Sciences*, Vol. 99, 2018, pp. 14–26.
- [16] Freydin, M., Keren-Rattner, M., Raveh, D. E., Kressel, I., Davidi, R., and Tur, M., “Fiber-Optics-Based Aeroelastic Shape Sensing,” *AIAA Journal*, Vol. 57, No. 12, 2019, pp. 5094–5103.
<https://doi.org/10.2514/1.J057944>
- [17] Nahom, T., Raveh, D. E., and Ivnovich, M., “Wind-Tunnel Study of the ARMA Flutter Prediction Method,” *Journal of Aircraft*, Vol. 56, No. 4, 2019, pp. 1441–1454.
- [18] Madenci, E., and Guven, I., *The Finite Element Method and Applications in Engineering Using ANSYS*, 2nd ed., Springer-Verlag, Berlin, 2015.
- [19] Drachinsky, A., and Raveh, D. E., “Aeroelastic Analysis of Very Flexible Wing Models Using the Modal Rotation Method,” *AIAA Journal* (in press).
- [20] ZAERO Theoretical Manual V. 9.2, Zona Technology, Scottsdale, AZ, 2017.
- [21] Peeters, B., Van der Auweraer, H., Guillaume, P., and Leuridan, J., “The PolyMAX Frequency-Domain Method: A New Standard for Modal Parameter Estimation?” *Shock and Vibration*, Vol. 11, 2004, pp. 395–409.
<https://doi.org/10.1155/2004/523692>
- [22] Towne, A., Schmidt, O. T., and Colonius, T., “Spectral Proper Orthogonal Decomposition and Its Relationship to Dynamic Mode Decomposition and Resolvent Analysis,” *Journal of Fluid Mechanics*, Vol. 847, May 2018, pp. 821–867.
- [23] Goizueta, N., Wynn, A., Palacios, R., Drachinsky, A., and Raveh, D. E., “Flutter Prediction for a Very Flexible Wing Wind Tunnel Test,” *Sci-Tech*, AIAA, Reston, VA, 2021.

S. Shin
Associate Editor